**Atmospheric
Chemistry
and Physics**

Characterization of Tropospheric Emission Spectrometer (TES) CO$_2$ for carbon cycle science

S. S. Kulawik[1], **D. B. A. Jones**[2], **R. Nassar**[2,3], **F. W. Irion**[1], **J. R. Worden**[1], **K. W. Bowman**[1], **T. Machida**[4], **H. Matsueda**[5], **Y. Sawa**[4], **S. C. Biraud**[6], **M. L. Fischer**[7], **and A. R. Jacobson**[8]

[1]Jet Propulsion Laboratory, California Institute of Technology, 4800 Oak Grove Drive, Pasadena, CA, 91109, USA
[2]University of Toronto, Department of Physics, Toronto, Ontario, Canada
[3]University of Toronto, Department of Geography, Toronto, Ontario, Canada
[4]National Institute for Environmental studies, 16-2 Onogawa, Tsukuba-City, Ibaraki, 305-8506, Japan
[5]Meteorological Research Institute, 1-1 Nagamine, Tsukuba-City, Ibaraki, 305-0052, Japan
[6]Lawrence Berkeley National Laboratory, Earth Sciences Division, Berkeley, CA, USA
[7]E. O. Lawrence Berkeley National Laboratory, Environmental Energy Technologies Division, Berkeley, CA, USA
[8]NOAA Earth System Research Lab, Global Monitoring Division, Boulder, Colorado, USA

Abstract. We present carbon dioxide (CO$_2$) estimates from the Tropospheric Emission Spectrometer (TES) on the EOS-Aura satellite launched in 2004. For observations between 40° S and 45° N, we find about 1 degree of freedom with peak sensitivity at 511 hPa. The estimated error is ∼10 ppm for a single target and 1.3–2.3 ppm for monthly averages on spatial scales of 20°×30°. Monthly spatially-averaged TES data from 2005–2008 processed with a uniform initial guess and prior are compared to CONTRAIL aircraft data over the Pacific ocean, aircraft data at the Southern Great Plains (SGP) ARM site in the southern US, and the Mauna Loa and Samoa surface stations. Comparisons to Mauna Loa data show a correlation of 0.92, a standard deviation of 1.3 ppm, a predicted error of 1.2 ppm, and a ∼2% low bias, which is subsequently corrected. Comparisons to SGP aircraft data over land show a correlation of 0.67 and a standard deviation of 2.3 ppm. TES data between 40° S and 45° N for 2006–2007 are compared to surface flask data, GLOBALVIEW, the Atmospheric Infrared Sounder (AIRS), and CarbonTracker. Comparison to GLOBALVIEW-CO$_2$ ocean

surface sites shows a correlation of 0.60 which drops when TES is offset in latitude, longitude, or time. At these same locations, TES shows a 0.62 and 0.67 correlation to CarbonTracker at the surface and 5 km, respectively. We also conducted an observing system simulation experiment to assess the potential utility of the TES data for inverse modeling of CO$_2$ fluxes. We find that if biases in the data and model are well characterized, the averaged data have the potential to provide sufficient information to significantly reduce uncertainty on annual estimates of regional CO$_2$ sources and sinks. Averaged pseudo-data at 10°×10° reduced uncertainty in flux estimates by as much as 70% for some tropical regions.

1 Introduction

Carbon dioxide (CO$_2$) is the most important anthropogenic greenhouse gas (IPCC, 2007). It is long-lived with a current global average tropospheric mixing ratio of about 390 parts per million (ppm), and is increasing at a rate of about 2 ppm per year. Superimposed on this upward trend is a seasonal cycle reflecting the uptake and release of CO$_2$ by the terrestrial biosphere and oceans, and which is markedly more

pronounced in the Northern Hemisphere than the Southern Hemisphere (Matsueda et al., 2002; Tans and Conway, 2005; Bösch et al., 2006). Currently about 55% of the anthropogenically emitted CO_2 remains in the atmosphere (IPCC, 2007, chapter 7), whereas the remainder is removed by the ocean and land biosphere; but the spatial and temporal distribution of the uptake has large uncertainties. Recent studies have shown that emissions of CO_2 from fossil fuel combustion have been increasing faster than predicted (Raupach et al., 2007) and that the southern hemispheric oceans' capacity for CO_2 uptake may be diminishing (Le Quéré et al., 2007). An improved quantitative understanding of the sources and sinks of atmospheric CO_2 is essential for reliably predicting future atmospheric CO_2 levels, for assessing the impact of land use changes on atmospheric CO_2, developing mitigation strategies, and for treaty verification.

Inverse modeling, which uses an atmospheric transport model to estimate fluxes from a set of atmospheric CO_2 observations, has emerged as an important tool for quantifying CO_2 sources and sinks. This approach, pioneered by Tans et al. (1990) and Enting and Mansbridge (1991), has become more sophisticated, but is limited by the fact that the current observational network is sparse and consequently does not have the information content to provide reliable constraints on carbon fluxes at regional scales (e.g., Rayner et al., 1996; Gloor et al., 2000; Suntharalingam et al., 2003). Studies using simulated data have demonstrated the potential utility of space-based measurements of CO_2 for providing improved estimates of regional CO_2 fluxes (e.g., Pak and Prather, 2001; Rayner and O'Brien, 2001; Houweling et al., 2004; Chevallier et al., 2007; Baker et al., 2006; Feng et al., 2009). For example, Rayner and O'Brien (2001) showed that satellite measurements of CO_2 column abundances with a precision of 2.5 ppm, averaged monthly and on spatial scales of $8° \times 10°$, would offer more information on CO_2 fluxes than can be obtained from the existing surface network. Houweling et al. (2004) showed that, with sufficient coverage, satellite observations of upper tropospheric CO_2 would lead to significant reductions of CO_2 source and sink errors as compared to the in situ observation network. Chevallier et al. (2005, 2009) found, however, that their inversions using upper tropospheric information from AIRS radiances are sensitive to latitude-dependent biases larger than about 0.3 ppm and that while their radiance assimilation improved surface flux uncertainties, it did not perform as well as the flask network. Baker et al. (2006) performed inversions of the same surface data using different models and found significant differences in flux estimates from transport error, suggesting measurements in the mid-troposphere would add value in addition to surface sites.

Space-based measurements of CO_2 are currently available from the Scanning Imaging Absorption Spectrometer for Atmospheric Chartography (SCIAMACHY), the Atmospheric Infrared Sounder (AIRS), the Infrared Atmospheric Sounding Interferometer (IASI), and the Greenhouse gases

Observing Satellite (GOSAT). SCIAMACHY was launched on the Envisat platform in 2001 and measures reflected sunlight at UV-SWIR wavelengths, with peak sensitivity near the surface. Buchwitz et al. (2005, 2007), Bösch et al. (2006) and Barkley et al. (2006) have presented daytime CO_2 retrievals over land from SCIAMACHY data. AIRS was launched on the EOS-Aqua platform in 2002 and different techniques have been used to retrieve atmospheric CO_2 abundances from AIRS radiances. These include using different spectral regions, different optimization methodologies, co-retrieving different species and direct assimilation of radiances. The different retrieval approaches have resulted in AIRS retrievals with estimated peak sensitivity ranging between 200 and 600 hPa (e.g., Chahine et al., 2005, 2008; Crevoisier et al., 2003; Engelen et al., 2004; Strow et al., 2008; Maddy et al., 2008). The AIRS data shown in this paper are taken from the AIRS standard product (Chahine et al., 2005, 2008). IASI, onboard the European MetOp platform, was launched in October 2006 and Crevoisier et al. (2009) have recently presented a tropical (20° N–20° S) ocean CO_2 product from IASI with peak sensitivity near 200 hPa. In January 2009, the GOSAT instrument was launched specifically to study greenhouse gases (http://www.jaxa.jp/projects/ sat/gosat/index_e.html) with a mission target of 4 ppm accuracy for a 3 month regional average using a combination of SWIR and IR channels (Hamazaki et al., 2004a, b; Yokota et al., 2009). The Orbiting Carbon Observatory (OCO) (Crisp et al., 2004) was lost as a result of a launch mishap in February 2009. This NASA satellite for dedicated CO_2 observations aimed to measure CO_2 columns with a precision of 1 ppm on regional, monthly scales (Crisp et al., 2004). OCO is now being rebuilt and is expected to relaunch in 2013.

We present here atmospheric CO_2 retrievals of the Tropospheric Emission Spectrometer (TES) satellite instrument. TES is a Fourier transform spectrometer that measures thermal infrared emission. We find that the TES nadir profile retrievals of CO_2 have peak sensitivity in the middle troposphere, near 500 hPa. The individual TES retrievals have errors of about 10 ppm at 511 hPa, but monthly averaging reduces the errors to about 1.3–2.3 ppm for $20° \times 30°$ and about 2 ppm for $10° \times 10°$. We show that TES CO_2 has the potential to reduce uncertainty in regional estimates of CO_2 fluxes through an observing system simulation experiment (OSSE). In a subsequent study by Nassar et al. (2010) we present an inversion analysis using the TES CO_2 data and compare the information provided by TES with that obtained from the in situ observing network for constraining CO_2 sources and sinks.

2 The TES instrument

TES is on the Earth Observing System Aura (EOS-Aura) satellite and makes high spectral resolution nadir measurements in the thermal infrared (660 cm^{-1}–2260 cm^{-1}, with

unapodized resolution of $0.06 \, \mathrm{cm}^{-1}$). It was launched in July 2004 in a sun-synchronous orbit at an altitude of 705 km with an equatorial crossing time of 13:38 (local mean solar time) and with a repeat cycle of 16 days. In standard "global survey" mode, 2000–3000 observations are taken every other day (Beer, 2006). There are additional targeted "special observations", which account for about 10% of TES data over mid-latitude Pacific in 2006, and which are not used in this analysis as they are less spatially and temporally uniform. TES level 2 data provide profile retrievals for atmospheric temperature (Herman et al., 2008), water (Shephard et al., 2008), HDO (J. Worden et al., 2007), ozone (H. Worden et al., 2007; Nassar et al., 2008; Osterman et al., 2008; Richards et al., 2008), carbon monoxide (Rinsland, 2006; Luo et al., 2007a, b), methane (Payne et al., 2009), as well as surface temperature, emissivity, and cloud information (Eldering et al., 2008). For details on the TES instrument, see Beer (2006), and for information on the retrieval process see Bowman et al. (2006) and Kulawik et al. (2006).

3 TES retrievals of atmospheric CO$_2$

3.1 Challenges of CO$_2$ retrievals

Estimating CO$_2$ from remote sensing measurements is challenging for a number of reasons. The horizontal variability of CO$_2$ at regional scales is small ($\sim$0.5%–3%) compared to most trace gases (e.g. ozone variability is $\sim$30%). Moreover, the spectral signature of CO$_2$ variations is small compared to spectral effects of temperature and water variability, as demonstrated in Fig. 1. As a result, CO$_2$ spectral lines are often used to estimate atmospheric temperature, where CO$_2$ concentrations are assumed to be fixed. Such an approximation is not valid for CO$_2$ retrievals, and could lead to a circular dependence between CO$_2$ and temperature. As shown in this paper, moderate temperature biases propagate into untenably large CO$_2$ errors, but this can be mitigated by jointly retrieving atmospheric temperature and CO$_2$ for monthly and regional averages.

Additionally, spectroscopic data used for infrared CO$_2$ retrievals are estimated to have $\sim$1% accuracy in the laser bands (around $1000 \, \mathrm{cm}^{-1}$) (Devi et al., 2003; Dana et al., 1992). While Devi et al. (2003) and Dana et al. (1992) agree within 1% for the laser bands, they both show a 4% bias with respect to previous work by Johns and Noel (1988), which indicates that biases on the order of 4% may also occur in the Johns and Vanderauwera (1990) measurements of the v_2 band (near $700 \, \mathrm{cm}^{-1}$). A 1% spectroscopy bias translates to a $\sim$4 ppm error in CO$_2$. On the positive side, a uniform bias could be easily corrected. Radiometric calibration and stability errors can propagate into the CO$_2$ retrievals; an effect which may not be noticed in the retrievlas of other more variable atmospheric constituents. Estimates of TES radiometric accuracy are 0.1 K (Kerola et al., 2009); this would result in
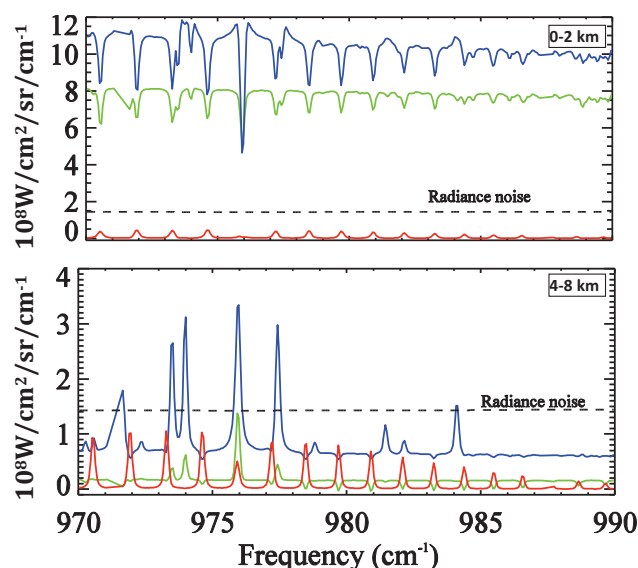
Fig. 1. Radiance change resulting from perturbations of +10% to water (blue), -1 K to atmospheric temperature (green) and 10 ppm to CO$_2$ (red). The perturbations are applied to the boundary layer (0–2 km) (top) and to the free troposphere (4–8 km) (bottom). The applied perturbations to water and temperature are of the same order as the predicted errors.

$\sim$2.5 ppm CO$_2$ error. However, if this is an RMS error, it averages out, whereas if it is a bias error, it can be corrected.

3.2 Retrieval setup

The development of TES CO$_2$ relied on a combination of guidance from validation with in situ CO$_2$ data and predictive calculations of error and information content which has been used to develop previous TES products, as described in Worden et al. (2004). The main validation data sets used were the Comprehensive Observation Network for TRace gases by AIrLiner (CONTRAIL) aircraft flask data, observations from the Mauna Loa and Samoa surface stations, and the SGP aircraft flask data (for land validation). A coarse vertical grid, consisting of 5 levels (surface, 511, 133, 10, and 0.1 hPa) was chosen for the retrieval, which minimizes contributions from the a priori state information at each retrieval level. The retrieved parameters for CO$_2$ are the logarithm of the volume mixing ratio at the above levels.

Testing was done with a prototype code based on the TES production code written in the IDL language (http://www.ittvis.com/ProductServices/IDL.aspx). Comparisons to validation data and examination of spectral residuals and other quality factors were used to iteratively update and refine the retrieval approach.

3.3 Retrieval methodology and error analysis

CO_2 is estimated by iteratively minimizing a cost function using the Levenberg-Marquardt non-linear least squares (NLLS) algorithm. The cost function, C(z), is the combination of the norm difference between the observed and predicted radiances and a penalty term based on the a priori knowledge of the atmosphere:

$$\mathbf{C}(z) = \|\mathbf{L}_{obs} - \mathbf{L}(z,b)\|^2_{\mathbf{S}_m^{-1}} + \|z - z_a\|^2_{\Lambda} \qquad (1)$$

L_{obs} is the observed radiance vector, which follows the additive noise model:

$$\mathbf{L}_{obs} = \mathbf{L}(z_{true}, b_{true}) + \varepsilon \qquad (2)$$

where ε is the radiance error. $\mathbf{L}(z,b)$ is the predicted radiance evaluated for the retrieved state z and non-retrieved state b. The cost function terms are weighted by the inverse of S_m (the radiance error covariance) and Λ (the constraint matrix). The constraint vector, z_a, is also used for the initial state. Note that $\|\mathbf{A}\|^2_B \equiv \mathbf{ABA}^T$.

When differences between radiances calculated at the true state and a priori vector are spectrally linear, the nonlinear retrieval can be represented by the linear equation:

$$\boldsymbol{x}_{est} = \boldsymbol{x}_a + \mathbf{G}\varepsilon + \mathbf{GK}_b(\boldsymbol{b}_{est} - \boldsymbol{b}_{true}) + \mathbf{A}(\boldsymbol{x}_{true} - \boldsymbol{x}_a) \qquad (3)$$

where $\mathbf{A}$ is the averaging kernel (which describes the sensitivity of the measurement to the true state), $\boldsymbol{x}_a$ is the a priori constraint vector, $\boldsymbol{x}_{true}$ is the true state, $\mathbf{G}$ is the gain matrix (describing the sensitivity of the measurement to changes in radiance), ε is the radiance error vector, $\mathbf{K}_b$ is the Jacobian matrix (describing the sensitivity of the radiance to each parameter, $\mathbf{K}^b_{ij} = \partial L_i / \partial b_j$) of the interferent parameters, and $\boldsymbol{b}$ are the interferent parameters.

The retrieved state $\mathbf{z}$ and the full state vector $\boldsymbol{x}$ (over which the forward model is calculated) are related through interpolation or mapping, and represent the log of the volume mixing ratio for CO_2. The retrieval algorithm is described in more detail in Bowman et al. (2006).

The second-order stochastic characterization of the atmospheric state and the spectral measurement noise are described by the a priori and measurement error covariances:

$$\mathbf{S}_a = cov(\boldsymbol{x}_{true} - \boldsymbol{x}_a) \qquad (4a)$$

$$\mathbf{S}_m = cov(\varepsilon) \qquad (4b)$$

Using Eq. (3), the covariance of the error between the retrieved and true state, $\mathbf{S}_{err} = cov(\boldsymbol{x}_{est} - \boldsymbol{x}_{true})$, can be calculated:

$$\mathbf{S}_{err} = \underbrace{\mathbf{GS}_m\mathbf{G}^T}_{\text{Measurement}} + \underbrace{\mathbf{GK}_b\mathbf{S}_{b\ err}(\mathbf{GK})^T}_{\text{Interferent}} \qquad (5)$$

$$+ \underbrace{(1 - \mathbf{A}_{xx})\mathbf{S}_{a,xx}(1 - \mathbf{A}_{xx})^T}_{\text{Cross} - \text{state}} + \underbrace{\mathbf{A}_{xy}\mathbf{S}_{a,yy}(1 - \mathbf{A}_{xy})^T}_{\text{Smoothing}} \qquad (5)$$

The measurement and interferent errors come from terms 2 and 3 of the right side of Eq. (3), respectively. The 4th term of Eq. (3) splits into "smoothing" and "cross-state" errors (which are described in Worden, 2004), where CO_2 indices are denoted by x, and the indices of co-retrieved species denoted by y. The cross-state component is due to the propagation of error from co-retrieved species into CO_2; these errors should decrease with target averaging over regional scales. However, when targets with the same true state are averaged, the smoothing term enters as a bias into the retrieved state and does not decrease with averaging.

The predicted total error covariance for an n target average is:

$$\mathbf{S}_{err} = (\mathbf{S}_{meas} + \mathbf{S}_{int} + \mathbf{S}_{cross-state})/n + \mathbf{S}_{smoothing}$$

$$\mathbf{S}_{err} = \mathbf{S}_{obs}/n + \mathbf{S}_{smoothing} \qquad (6)$$

The observation error and smoothing error covariances in Eq. (5) are included in the TES products (Osterman et al., 2009). The predicted error for a particular level is the square-root diagonal of the predicted error covariance at that level, and the off-diagonal terms describe correlated errors between levels. Spectroscopic and calibration errors, which may contribute an additional bias and/or random error, are not included in Eq. (5).

3.3.1 The observation operator

The TES averaging kernel and a priori constraint vector are used in the "observation operator", $\mathbf{H}(*) = \boldsymbol{x}_a + \mathbf{A}(* - \boldsymbol{x}_a)$ (Jones et al., 2003). This estimates a TES measurement of CO_2 given an input CO_2 profile $\boldsymbol{x}$, which may be derived from an in-situ measurement or a model forecast:

$$\boldsymbol{x}_{obs} = \boldsymbol{x}_a + \mathbf{A}(\boldsymbol{x} - \boldsymbol{x}_a) \qquad (7)$$

This operator uses the sensitivity calculated in the averaging kernel which is provided in the TES standard product. When a TES measurement is compared to $\boldsymbol{x}_{obs}$, the expected discrepancy is the "observation error" which is the sum of the measurement error, interfering species error, and cross-state error, shown in Eq. (5), and provided in the TES standard product.

3.4 The predicted sensitivity

The approximations assumed in the linear retrieval in Eq. 3 can be validated, as described in Kulawik et al. (2008), by comparing non-linear retrievals using two different a priori vectors, $\boldsymbol{x}_a$ and $\boldsymbol{x}_a'$. The non-linear retrieval using $\boldsymbol{x}_a'$ is compared to the non-linear retrieval using $\boldsymbol{x}_a$ followed by a linear
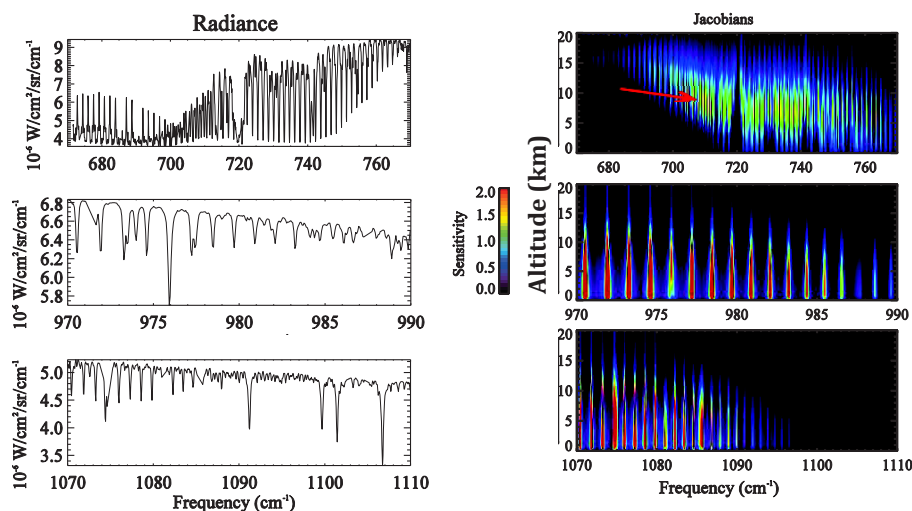
Fig. 2. Radiances and Jacobians for the three CO$_2$ bands used in the retrievals. The Jacobians show the sensitivity of radiances to changes in CO$_2$ at different altitudes. The red arrow shows the sensitivity of the radiance at 710 cm^{-1} when CO$_2$ at 10 km is changed. The Jacobians have been divided by the radiance noise, so a value of 1 means that the radiance will change by the same amount as the expected radiance noise.

transformation of the a priori vector from x_a to x_a' using the expression:

$$x_{est}' = \hat{x} + A(x_a' - x_a) \tag{8}$$

where $\hat{x}$ is the non-linear retrieval obtained with x_a, and x_{est}' is the linear estimate of the NLLS retrieval with a priori vector x_a'. x_{est}' from Eq. (8) can be compared to the $\hat{x}'$, the non-linear retrieval obtained using a priori vector x_a'. This analysis is done in Sect. 5.4.

3.5 Radiances and Jacobians

TES filters used in normal operation span the spectral region from 660 cm^{-1} to 2260 cm^{-1}, with gaps from 910–950 cm^{-1} and 1320–1891 cm^{-1}. There is significant CO$_2$ signal in the radiance between 660–770 cm^{-1}, 930–1090 cm^{-1} and near 2100 cm^{-1}. The signal near 2100 cm^{-1} has a low signal to noise ratio and was not used, and 990–1070 cm^{-1} was excluded because of interference from the 10 μm ozone band. Figure 2 shows the radiance and Jacobians for the three CO$_2$ sensitive spectral regions considered. Although the v_2 band (near 700 cm^{-1}) has a stronger spectral signature, the laser bands (near 1000 cm^{-1}) have similar information content due to a better signal to noise ratio.

The mean and standard deviation of radiance residuals, which is the difference between the observed and forward model spectra, following CO$_2$ retrievals highlight problematic spectral lines and regions. Spectral regions with standard deviation >1.2 × the NESR (Noise Equivalent Spectral Radiance), or with mean residual >0.5 × the NESR for a large set of retrievals were taken from the window list. The impact on CO$_2$ sensitivity was minor (less than 0.05 DOF). The full window list is shown in Table 1.

Table 1. Spectral windows used for TES CO$_2$.

TES filter	Start (cm^{-1})	End (cm^{-1})
2B1	671.620	673.420
2B1	674.020	685.300
2B1	685.840	690.100
2B1	690.580	697.180
2B1	697.660	705.100
2B1	705.580	713.201
2B1	713.740	713.800
2B1	714.280	723.220
2B1	723.701	724.960
1B2	967.100	971.060
1B2	971.660	987.260
1B2	987.740	990.02
1B2	1070.000	1073.720
1B2	1074.200	1074.680
1B2	1075.280	1080.980
1B2	1081.520	1085.120
1B2	1085.780	1104.620
1B2	1105.160	1117.400

The species included in the forward model were H$_2$O, CO$_2$, O$_3$, HNO$_3$ for the 2B1 filter and H$_2$O, CO$_2$, O$_3$, CFC-11, CFC-12 for the 1B2 filter.

3.6 Retrieval strategy

In light of the impact of CO$_2$ of errors in temperature and water, the retrieval strategy selected jointly retrieves atmospheric temperature, surface temperature, emissivity (over

Table 2. Degrees of freedom for CO_2 for one ocean target in different scenarios.

	CO_2 alone	$+T_{ATM}$	$+H_2O$	+clouds, TSUR
ν_2	1.87	1.00	0.62	0.61
laser	1.02	0.88	0.72	0.68
ν_2 + laser	2.08	1.33	1.09	1.04
Sel. Windows	1.94	1.22	1.01	0.95

Additional retrieval species are added in each column, so the final column retrieves CO_2, atmospheric temperature, water, clouds, and surface temperature. The "ν_2" window is 670–775 cm^{-1}, the laser windows are 967–990 and 1070–1117, and the selected windows are shown in Table 1. Note that additional windows to improve temperature and water would increase the CO_2 DOFs in a joint retrieval with the upper limit being the "CO_2 alone" column.

land), water vapor, and CO_2. For water, the constraints and retrieval are the same as those used operationally for TES, however the emissivity constraint was updated to allow more variation in emissivity. The temperature constraint was also tightened from ~2 K to ~0.6 K variability to allow more degrees of freedom for CO_2 and which matches TES-sonde temperature biases of ~0.5 K (Herman et al., 2008). Ozone was not jointly retrieved as it was found that retrieving ozone had no impact on the carbon dioxide monthly average values.

Table 2 shows the total degrees of freedom with different TES spectral windows and different species combinations. Table 2 shows that if CO_2 were retrieved by itself, i.e. assuming temperature and water are adequately known, CO_2 would have more than double the degrees of freedom as when it is co-retrieved with temperature and water. However, as shown in the next section, the temperature must have a low average bias for this strategy to work. Table 2 also shows that the laser bands contain more independent CO_2 information as compared to the ν_2 band (by comparing rows 1 and 2) and that only about 0.1 additional degree of freedom is available for CO_2 beyond the windows selected (by comparing rows 3 and 4). The degrees of freedom available for CO_2 would also increase if more windows are included which independently determine temperature, water, etc., effectively freeing up shared information for estimating CO_2. However since calibration and spectroscopy vary for TES for different filters and spectral regions, a working strategy implementing this has not been developed. Additionally, averaging strategies which reduce measurement error could improve CO_2 sensitivity.

3.7 A priori covariance and constraint

The a priori covariance, used for calculating the smoothing error, is set to the same values globally, although the atmospheric variability of CO_2 is significantly lower in the Southern Hemisphere. The square root values of the diagonal of the a priori covariance are set to: 4, 3.5, 2.5, 2, and 2 ppm at

the surface, 511, 133, 10, and 0.1 hPa, respectively. The surface variability is based on the average GLOBALVIEW variability (3.5 ppm variability) which is increased to 4 because of the higher variability over land (e.g. 10 ppm variability for SGP aircraft data). The 511 hPa variability is based on measurements of Mauna Loa variability. The 133 hPa variability is based on CONTRAIL variability, and the values at the higher levels are slightly reduced from the CONTRAIL variability. The off-diagonal correlations in the a priori covariance matrix are 0.8 for the first two levels, based on correlations of monthly averaged SGP data for the first two levels, 0.9 for the second two levels, based on correlations of Mauna Loa and CONTRAIL data, and 0.9 for all other adjacent levels.

As seen in Eq. (1), the constraint matrix determines how much weight is given to the a priori knowledge of the atmosphere. The relative constraint strengths for CO_2 and temperature also determine the partitioning of shared degrees of freedom between CO_2 and temperature. The selection of a reduced set of retrieval levels or linearly scaling a profile can also be represented in the a priori framework and expressed as a constraint matrix. The effect of the constraint can be seen by applying the observation operator (Eq. 7) to a model or aircraft profile to simulate the degraded vertical resolution seen by TES.

The constraints are calculated based on the method of Kulawik et al. (2006) with the variability of the CO_2 covariance, which is discussed in Sect. 4, enhanced to 5.4% at the surface and 2.8% in the mid-troposphere which increases both the sensitivity to CO_2 and the measurement error. As seen in Sect. 5, this loose constraint results in a large uncertainty for a single target and a 1.3–2.3 ppm error with averaging.

4 In situ observations of atmospheric CO_2

4.1 In situ and other datasets used for validation of TES CO_2

TES CO_2 data over oceans for the period 2005–2008 are compared to CONTRAIL data and to surface data from Samoa and Mauna Loa. The CONTRAIL dataset contains in situ aircraft flask measurements taken on commercial flights between Australia and Japan. The data are collected primarily between 10–11 km one to two times per month at 12 latitudes between 24° S and 35° N (Matsueda et al., 2002, 2008; Machida et al., 2008). The CONTRAIL dataset is extremely useful for satellite validation as it occurs in the upper troposphere over all seasons in both the Northern and Southern Hemispheres. We compare to sets of CONTRAIL data in the Northern Hemisphere between 13°–35° N, and in the Southern Hemisphere between 10°–25° S. We also compare to the Mauna Loa site, which is at 3.4 km altitude, 19.5° N, 155° W and is part of the NOAA Earth System Research Laboratory (ESRL)/Global Monitoring Division

(GMD) Carbon Cycle Greenhouse Gases network (http://www.esrl.noaa.gov/gmd/ccgg/index.html). This site is useful as it has monthly averaged data at an altitude somewhat lower but comparable to the location of peak sensitivity of TES, at 5 km. The GMD Samoa site (54.5° S, 154° E) provides surface measurements complementary to the Southern Hemisphere CONTRAIL data. Together these data bracket the altitudes of the peak TES sensitivity. A map of validation sites and coincident TES observation locations shown in Fig. 3. In the Pacific, we also compare to the AIRS CO_2 dataset (Chahine et al., 2005, 2008), which monthly averages gridded by 2°×2.5°, available from http://mirador.gsfc.nasa.gov/ (keyword AIRX3C2M). The retrieved parameter is a scaling factor applied to a CO_2 profile and has peak sensitivity at 300 hPa for mid-latitudes (Olsen, 2009).

For validation of the TES data over land for 2006–2008, we compare to aircraft flask measurements taken at the Southern Great Plains (SGP) Atmospheric Radiation Measurement (ARM) site with up to 12 measurements between 0.3 and 5.3 km altitude up to 8 times per month. This site is located in the southern United States at 36.8° N, 97.5° W, and has data starting in 2006.

For TES CO_2 retrievals between 40° S and 45° N, we compare to surface station flask data from the NOAA GMD network (Conway et al., 2008), the GLOBALVIEW dataset (GLOBALVIEW-CO_2, 2008), and CarbonTracker (Peters et al., 2007; http://carbontracker.noaa.gov). The GLOBALVIEW dataset interpolates and extends data from surface and aircraft flask measurements, and continuous surface and tower CO_2 measurements to provide weekly CO_2 values at specific locations (Masarie and Tans, 1995). There are 39 stations (25 ocean and 14 land) between 35° S and 40° N with data in 2006–2007, although some do not have continuous data. Ocean sites are expected to compare better with TES measurements because of smaller differences in CO_2 between the surface and free troposphere. CarbonTracker is a data assimilation system that combines in situ observations with a model to produce three dimensional estimates of tropospheric CO_2 distributions as well as estimates of sources and sinks. The CO_2 distributions have global, daily output on 34 pressure levels ranging from the surface to 0.1 hPa. TES is compared to CarbonTracker at the surface and at 500 hPa with and without the TES averaging kernel.

4.2 Observed variability in CO_2 at the surface and in the free troposphere

This section compares in situ data at different locations and altitudes to provide context for the TES results. Surface station flask data show seasonal variability of 2–15 ppm, with larger variability observed over land and in the Northern Hemisphere, and the highest seasonal variability towards the north pole. Over the northern mid-latitude Pacific Ocean, comparisons were made between monthly averaged surface data from the Guam ground station (at 13.7° N, 144° E),
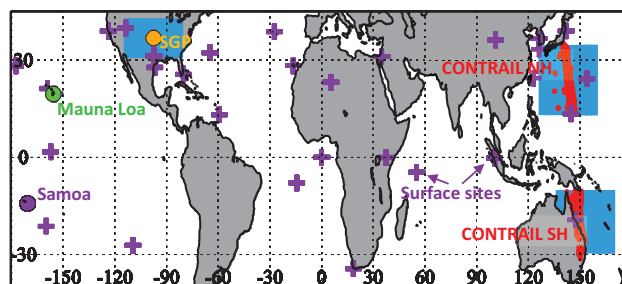

Fig. 3. Validation locations: In the Northern Hemisphere, CONTRAIL data (red dots, 13°–35° N, ~140° E, 10–11 km) are compared to TES in the same vicinity (blue, 13°–35° N, 128°–158° E). The same TES data are compared to Mauna Loa observatory (green, 19.5° N, 155° W at 3.4 km). Over land, TES (28.8°–44.8° N, 109.8°–85.5° W) is compared to aircraft data at the Southern Great Plains (SGP) ARM site in the US (orange, 36.8° N, −97.5° W, 0.5–5.3 km). In the Southern Hemisphere CONTRAIL data (red dots, 10°–30° S, ~150° E, 10–11 km) are compared to TES data from the box (10°–30° S, 128°–168° E). These are also compared to the Samoa surface site (purple circle, 14° S, 170° W). TES data between 40° S and 45° N are also compared to the GLOBALVIEW dataset (purple +'s).

CONTRAIL aircraft flask data at 10–11 km, and the Mauna Loa ground station (at 3.4 km elevation). There is good agreement at these different longitudes, latitudes, and altitudes (with perhaps a one-month temporal lag in CONTRAIL for January through April). This indicates that CO_2 over the Pacific is fairly uniform in latitude (between 15°–35° N), longitude, and altitude (between 0–12 km). The seasonal cycle is about 5 ppm in these data.

In contrast, aircraft measurements taken at the SGP site in the southern United States show a seasonal variability of ~10.0 ppm between 0–2 km, with a seasonal pattern peaking earlier than at Mauna Loa. In contrast, the 2–7 km data from the SGP have ~5 ppm seasonal variability with a similar seasonal pattern to Mauna Loa. Variability within each month drops off with altitude with intra-monthly variability of 3.9 ppm for the 0–2 km data. For the 2–4 km data and the 4–7 km data, the intra-monthly variability is 1.8 ppm and 1.4 ppm, respectively. The 2–4 km and 4–7 km data showed similar seasonal patterns.

In the southern Pacific Ocean, the Samoa ground station and CONTRAIL aircraft data between 10–30° S both show ~3 ppm seasonal variation, with Samoa showing an irregular monthly increase, and CONTRAIL perhaps showing a peak around July of each year. Both show variability within each month of ~0.5 ppm. A surface station at Cape Ferguson, Australia (19° S, 147° E), close to the CONTRAIL flight path, shows the same yearly increase with different monthly variability. The CONTRAIL data, on average, have a 0.5–1 ppm high bias versus the surface stations, which, when looking at data averaged over several years, appears to occur between May and August. In summary, the Southern
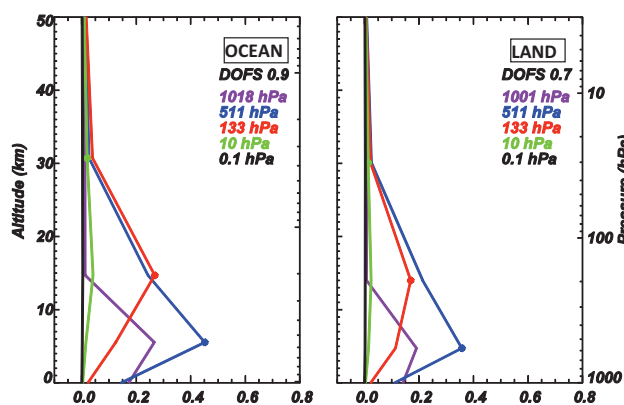
Fig. 4. Averaging kernel rows for an average of ocean (near Mauna Loa, left) and land (near the SGP site, right) targets over a 4-year period. The ocean targets show more sensitivity on average because the mean tropical ocean temperature is 300 K versus 290 K for the land cases, leading to a higher thermal contrast. Therefore, although daytime, summer, land targets will have the greatest sensitivity, averaging over winter and night reduces land average sensitivity.

Hemisphere shows little seasonal variability, but there are month by month differences between the surface data and CONTRAIL.

5 Characterization of results

### 5.1 Sensitivity and errors of a single target

Averaging kernel rows for Ocean (in Pacific Ocean, 13°–35° N) and Land (near SGP, 31°–46° N) retrievals are seen in Fig. 4. Thermal contrast drives the sensitivity of the retrievals in the infrared, with higher sensitivity correlated with higher surface temperatures. Summertime, daytime, land cases have the most sensitivity, however tropical ocean locations have more sensitivity than land locations when averaged over day and night, and all seasons. The averaging kernels show sensitivity for the retrieved value at the surface, 511 hPa, and 133 hPa. The peak sensitivity is at 511 hPa with about 45% sensitivity near the 511 hPa level, about 10% sensitivity near the surface, and about 25% sensitivity around the 133 hPa level, with the remainder coming from the prior.

Figure 5 shows the predicted errors for both a single target and a 100-target average for TES CO_2 retrievals. The single target predicted error is about 6 ppm at 511 hPa, which is dominated by cross-state error, primarily from atmospheric temperature, but also from water, surface temperature, and cloud properties. The 100-target average error at 511 hPa is about 1.4 ppm, dominated by the smoothing error.

The thermal infrared radiation signal strength observed by TES depends on the surface temperature and surface properties. As a result, sensitivity to CO_2 depends on latitude as shown in Fig. 6. Because of the sensitivity decrease with
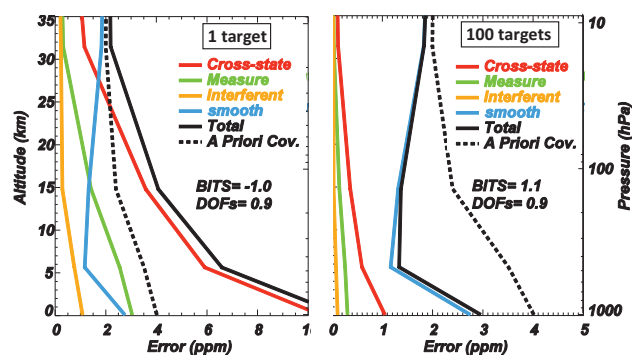
Fig. 5. Errors for a single target (left) and a 100-target average (right). For the single target, the dominant error is the cross-state error, which results from the propagation of errors from temperature, water, surface temperature, and clouds into CO_2. For the 100-target average, all errors except for self-smoothing, which results from sub-optimal sensitivity, are assumed to add randomly. Self-smoothing is the dominant error for the 100-target average.
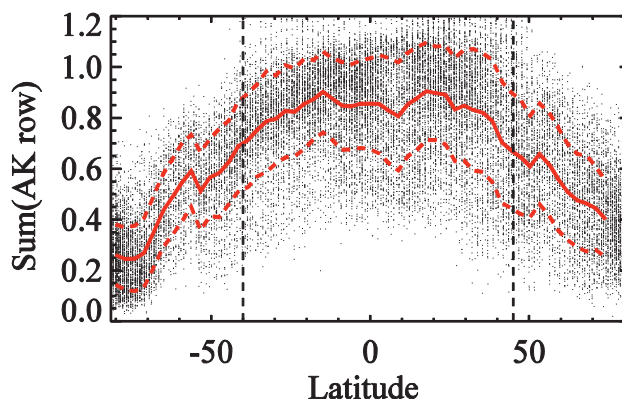
Fig. 6. Sensitivity vs. latitude of the TES CO_2 retrievals in October 2006. Since the sensitivity drops off with latitude, only targets between 40° S to 45° N are processed to retrieve CO_2.

higher latitudes, only 40° S to 45° N is used from TES data. Results at higher latitude do not compare well to aircraft validation data at 65° N at Poker Flats (not shown). For similar reasons, only targets with cloud optical depth (OD) less than 0.5 are considered to have good quality.

5.2 Predicted and actual errors for averaged profiles

In this section we test Eq. (6) by calculating the actual and predicted errors for various numbers of averaged profiles in boxes of 10°×10°, 15°×15°, 20°×20°, and 20°×30° degrees. Three years of TES data are compared to Mauna Loa (with and without the TES observation operator) and CONTRAIL data as shown in Fig. 7. All comparisons show a decrease in error as the number of profiles averaged increase, as predicted. Equation 6 suggests that the error of TES versus Mauna Loa or CONTRAIL should fit to $\sqrt{\mathbf{S}_{obs}/n + \mathbf{S}_{smoothing}}$

and the error of TES versus Mauna Loa with the TES observation operator should fit to $\sqrt{S_{obs}/n}$. Fits of the data shown in Fig. 7 to the form of Eq. (6) indicated that the observation error is 12.3 ppm (rather than the predicted 6 ppm) and the smoothing error is 1.1, about as predicted. The largest uncertainty in the smoothing error is the a priori covariance, which predicts the initial uncertainty in the atmospheric state. The dominant error of observation error is the cross-state error, which includes temperature and water errors. CO$_2$ error is not found to be very sensitive to the initial water uncertainty but increasing the temperature a priori uncertainty from about 2 K to 5 K resulted in a 12 ppm predicted error for CO$_2$. However, 5 K is larger than the expected initial error in TES temperature, and this suggests another source of error for CO$_2$, e.g. a variable calibration error, which averages out similarly to the observation error.

5.3 Impact of temperature and cloud errors

The effects of temperature errors were studied by setting the temperature to the initial guess or the initial guess perturbed by +0.1 K throughout the profile. The difference in retrieved CO$_2$ (holding temperature fixed) for the two initial temperature values was calculated and compared to the predicted change using Eq. (3). Based on a case study of about 100 non-linear retrievals, it was found that a +0.1 K temperature error resulted in a +2.5 ppm CO$_2$ error. This agreed with the predicted propagation of temperature error, as given by the quantity $\mathbf{GK}_b$ (0.1 K) from Eq. (3). As the uncertainties in the TES initial temperature (from NASA's Global Modeling and Assimilation Office GEOS-4 meteorological fields) are $\sim$2 K compared to sondes (Herman et al., 2008), temperature errors resulting from fixing the temperature to the initial value would translate into unacceptable errors in CO$_2$, of up to 50 ppm, for a single target. However, when temperature and water are jointly retrieved along with CO$_2$, the temperature and water errors partially cancel, and result in predicted errors of $\sim$6 ppm for a single target, and less when averaged over many targets.

With the cloud optical depth (OD) less than 0.5, the predicted errors from clouds propagated to CO$_2$ are on the order of 1 ppm. We would expect this to impart a random error with some targets retrieving clouds that are too optically dense, and other targets retrieving clouds that are too optically thin. The systematic impact of cloud errors was studied by comparing TES versus Mauna Loa data for different retrieved cloud top pressures and cloud optical depths. The targets were divided into two groups, those with OD<0.1 (162 targets per monthly average) and those with OD between 0.1–0.5 (101 targets per monthly average). The predicted DOF is 0.85 versus 0.67 for these targets and the RMS errors versus Mauna Loa data with the TES observation operator are 1.3 and 1.5 ppm, respectively. Although OD<0.1 performs better, averaging all cases results in a lower RMS of 1.1 ppm due to averaging more targets. The two cloud
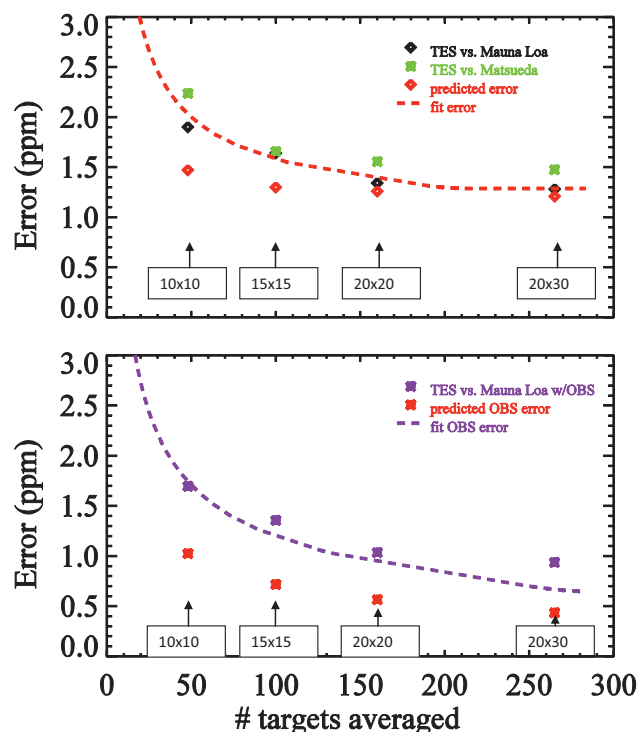

Fig. 7. Actual and predicted total error (top panel) and observation error (bottom panel). The actual error is the root mean square difference between TES and in situ data. As predicted, comparisons to in situ data improve as the number of profiles averaged increases. The actual error fits best to an observation error of 12 ppm (about twice the predicted observation error) and a self-smoothing error of 1.1 ppm (as predicted). This fit is shown as a red dashed line in both panels.

bins show a relative bias of 0.6 ppm (higher cloud OD results in higher CO$_2$). Partitioning cases with clouds (OD>0.1) into those with cloud top pressures greater than and less than 500 hPa, produced 53 and 54 targets per bin, respectively. The RMS errors for these cases, based on comparison to Mauna Loa data with the TES observation operator, were 1.9 and 1.7 ppm, respectively, with a relative bias of 1.9 ppm (higher altitude clouds result in higher CO$_2$ retrieved). These values indicate that cloud optical depth artifacts are likely not a concern, but that cloud pressure artifacts may be impacting CO$_2$ retrievals and should be further studied. By itself this result should not be used to screen TES data based on cloud pressure, since cloud properties are related to convective processes and vertical transport, which can result in differences in atmospheric composition.

5.4 Validation of predicted sensitivity

Starting the retrieval with a different prior and initial guess is used to validate the averaging kernel and retrieval linearity. TES data in the Northern Hemisphere Pacific Ocean (13–35° N, 128–158° E) were processed using both a 360 ppm
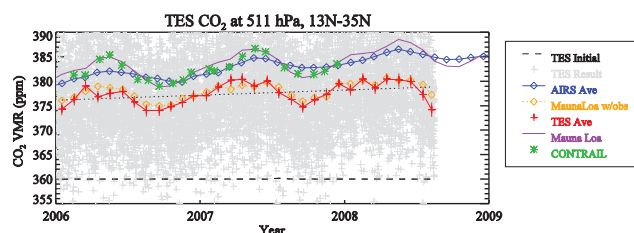
Fig. 8. TES CO_2 retrieved with an initial guess and prior (dashed line) of 360 ppm for (13-35° N, 128-158° E). The TES results (red) agree well with Mauna Loa data with the TES observation operator (orange) applied, which accounts for TES sensitivity. This validates the TES reported sensitivity, which is captured in the averaging kernel.

(360IG) and a 380 ppm (380IG) initial guess and prior value (both the a priori vector and initial guess are set to the specified values for all pressures and all dates) for 2006–2008. The two sets of retrievals are compared to Mauna Loa data to determine the effect of starting at a "bad" initial guess and prior, and compared to each other to determine if they are consistent given the TES predicted sensitivity. Figure 8 shows 360IG compared to Mauna Loa with the TES observation operator (Eq. 7). The consistency of these results validate TES's averaging kernel, with the averaging kernel row at 511 hPa averaging ~0.8. However, 380IG correlates somewhat better than 360IG with Mauna Loa (r=0.95 versus r=0.91), showing that the initial guess and prior do make some difference in the resulting accuracy. Monthly averaged 380IG values were converted using Eq. (8) to a 360 ppm a priori vector to create the 360EST dataset. The 360EST dataset averaged 1.2 ppm higher than 360IG, with a 0.8 ppm rms. The bias between 360EST and 360IG is likely due to the smaller degrees of freedom (by 0.05) for 360IG, reflecting the fact that the averaging kernel is calculated at the retrieved state, which is lower for 360IG.

Conversion using the averaging kernel on the TES 66-level pressure grid instead of the 5-level CO_2 retrieval level grid yielded similar results. Applying Eq. (8) to individual targets and then creating monthly averages yielded a larger standard deviation (4 ppm vs. 0.8 ppm) and a smaller bias (0.4 ppm vs. 1.2 ppm) versus first averaging and then converting with Eq. (8). Operationally, the initial error is not expected to be more than 5 ppm. These findings validate the reported sensitivity and indicate that the results are fairly robust under changes to the a priori vector (e.g., as described in Kulawik et al., 2008).

5.5 Bias characterization

TES results show a low bias of about 6 ppm relative to all validation data, which is most likely due to some combination of calibration and spectroscopic error. The bias changes when the spectral windows or constraints are changed. This bias,

however, appears to be stable over the 3 years of uniformly processed data using TES v003 radiances. Whether the bias is spectroscopic or calibration, it can be represented as a radiance error which propagates into CO_2 using the equation $\Delta \boldsymbol{x} = \mathbf{G} \Delta \mathbf{L}$, where $\Delta \boldsymbol{x}$ is the error in log(VMR), $\mathbf{G}$ is the gain matrix, and $\Delta \mathbf{L}$ is the radiance error. If it is from a line intensity error, the Jacobian error is of the form $\Delta \mathbf{K} = f \mathbf{K}$, making the radiance error $\Delta \mathbf{L} = f \mathbf{K} \boldsymbol{x}$, where $\boldsymbol{x}$ is the log of the true state, so the error in the retrieved value is $f \mathbf{A} \boldsymbol{x}$. This is the format assumed for the error. The value for f was set by comparisons to data from the Mauna Loa observatory, as these data had the highest correlation with the retrieved TES values. The best fit for f was 0.021, or 2.1%. Applying the correction factor did not impact the correlation but did improve the bias. TES v004 radiances, which have an update to the frequency calibration, had a similar but slightly larger bias of about 0.023. Ideally the comparison would be to oceanic well-mixed aircraft data covering the altitudes of TES sensitivity (surface through ~11 km) with the TES observation operator applied rather than to a uniform profile set to the Mauna Loa surface value with the TES observation operator applied. However, this correction factor is easy to update, as it is applied post-processing using the averaging kernels in the product.

6   Comparisons to in situ data, AIRS, and CarbonTracker

The validation dataset for CO_2 is far more comprehensive than for many other atmospheric constituents. We compare to 39 surface stations between 35° S and 40° N, which report daily or monthly values, to aircraft data taken over the United States (SGP) and to aircraft data taken in the Pacific between Japan and Australia (CONTRAIL), data from the AIRS instrument, and to CarbonTracker.

### 6.1   CONTRAIL, Mauna Loa, and AIRS in the Northern Hemisphere

In Fig. 9 we compare CONTRAIL aircraft measurements of CO_2 in the Northern Hemisphere to TES data processed from the same vicinity, with locations described in Fig. 3. The TES data are also compared to data from the Mauna Loa surface site and to AIRS measurements from the same latitude and longitude ranges as TES. The Mauna Loa and CONTRAIL data, at 3.5 and 10.5 km, respectively, are useful in that they bracket the altitude of maximum TES sensitivity, around 5 km. The AIRS CO_2 used (Chahine et al., 2005) has peak sensitivity around 300 hPa, corresponding to a higher altitude than TES CO_2. Figure 9 shows a time series of the datasets (top panel), the difference between TES and Mauna Loa with the TES observation operator (middle panel), and correlations of TES to the other measurements (lower panel). For the application of the TES observation operator, the true
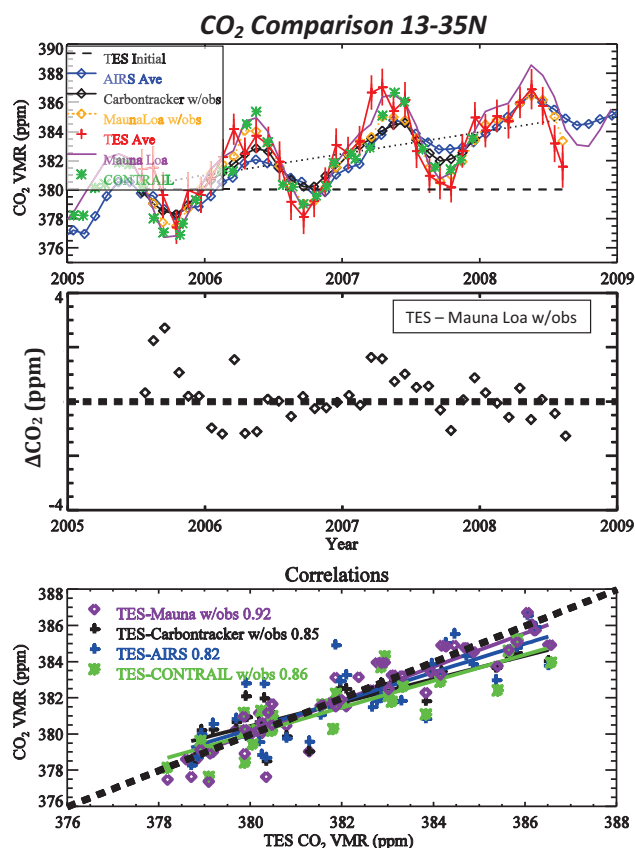
Fig. 9. Comparison of TES (at ~5 km, red), Mauna Loa surface data (at 3.5 km, purple), CarbonTracker (5 km), AIRS (~9 km, blue), and CONTRAIL aircraft data (10-11 km, green) in the Northern Hemisphere (13°–35° N, 128°–158° E). The top panel shows a time series of the different datasets, where the TES initial and a priori values are set to 380 ppm (dashed line). The orange data show the observation operator applied to Mauna Loa, which agrees best with TES data as the TES averaging kernel row sums to about 0.8. The middle panel shows TES – Mauna Loa with TES observation operator, which does not show a trend. The bottom panel shows TES (x-axis) plotted versus the above data.

value is set to the Mauna Loa value for all pressures. TES is most correlated with Mauna Loa ($r=0.92$) and Carbon-Tracker ($r=0.95$) and correlated with CONTRAIL and AIRS at about $r=0.85$. The correlations represent a combination of yearly and seasonal trends.

As seen in Fig. 9 TES begins to show a low bias versus Mauna Loa without the TES observation operator, starting in mid-2008, when CO$_2$ deviates significantly from the a priori value of 380 ppm. The bias is improved with the application of the TES observation operator, which takes into account the TES sensitivity. For assimilation of data, it is most important to have the sensitivity accurately characterized, as demonstrated by the good comparison of the TES average (red) and Mauna Loa with TES observation operator (orange).
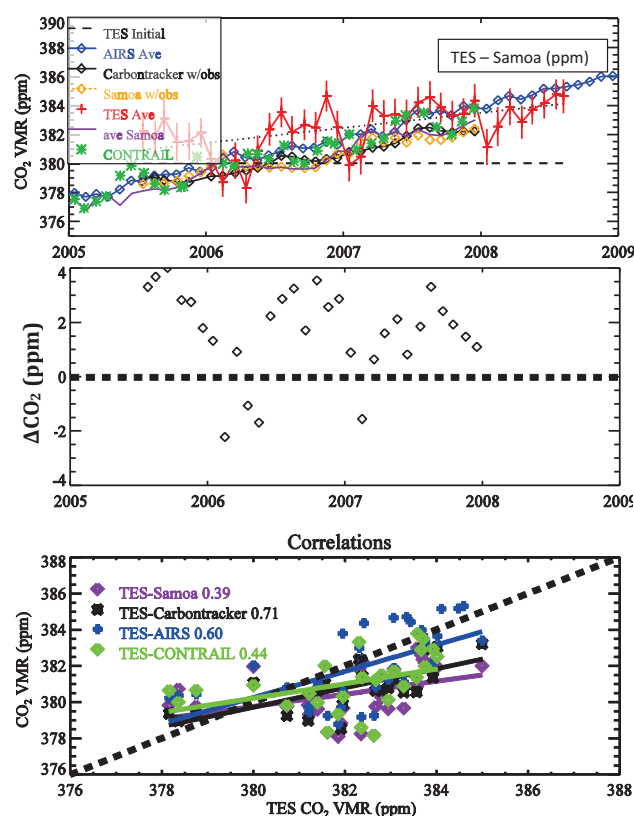
Fig. 10. Comparison of TES (at ~5 km, red), Samoa surface data (purple), CarbonTracker (5 km), AIRS (~9 km, blue), and CON-TRAIL aircraft data (10–11 km, green) in the Southern Hemisphere (10°–30° S, 128°–168° E). The top panel shows a time series of the different datasets, where the TES initial and a priori values are set to 380 ppm (dashed line). The middle panel shows TES – Samoa with TES observation operator. The bottom panel shows TES (x-axis) plotted versus the above data.

6.2 CONTRAIL, Samoa, AIRS in the Southern Hemisphere

As seen in Fig. 10, the seasonal variability of Southern Hemisphere CO$_2$ is far less than the Northern Hemisphere, although the yearly increase in CO$_2$ is similar in both hemispheres. Figure 10 shows comparisons of CONTRAIL, AIRS, CarbonTracker, and the Samoa surface site with TES based on the locations as described in Fig. 3. The TES variability is larger than expected as compared to the validation data, with high values in the second part of the year, particularly in 2005 and 2006, which show up clearly in Fig. 11. Correlations with CONTRAIL, AIRS, and Samoa are shown in Fig. 10, as well as the bias versus Samoa over time. To understand the differences between TES and the validation data we also looked at data from the Rarotonga aircraft site in the Southern Hemisphere at 21° S, 160° W. Although missing data for much of 2005–2006, Rarotonga aircraft data are 1–2 ppm higher at 4.5 km than at 0.5 km, indicating that the
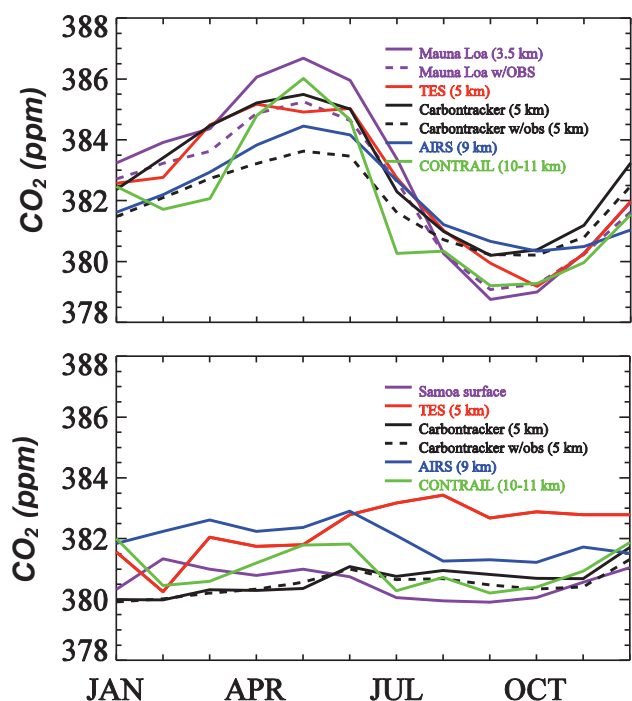
Fig. 11. Monthly averaged CO_2 July 2005 to July 2008 in the Northern Hemisphere (top panel) and Southern Hemisphere (bottom panel). In the Northern Hemisphere, the agreement is generally within 2 ppm for all datasets, with Mauna Loa showing the most seasonal variability and TES versus Mauna Loa with the TES observation operator applied showing the best agreement. In the Southern Hemisphere, TES values are ~2 ppm high compared to Samoa and CONTRAIL in the second half of the year which is discussed in the text.

southern Pacific is not as vertically homogenous as the northern Pacific.

6.3 Seasonal variations from 2005–2008 monthly averages

Figure 11 shows the seasonal variability of the observations, based on three years of data, from June 2005 to June 2008, averaged by month (i.e. all data from August 2005, 2006, and 2007 averaged. In the Northern Hemisphere, TES agrees well with the Mauna Loa data transformed with the TES observation operator,which has less seasonal variability than the raw Mauna Loa data. CarbonTracker shows a similar seasonal pattern with less variability, especially considering that the data do not have the TES observation operator applied. AIRS, at a higher altitude, shows the same seasonal pattern with less variability. The CONTRAIL data, at 10–11 km, appear to show approximately the same seasonal variability as Mauna Loa, with faster transitions. In the Southern Hemisphere, the seasonal variability of all datasets is markedly less, and the agreement is less striking. TES shows higher values in the second half of the year, with a seasonal
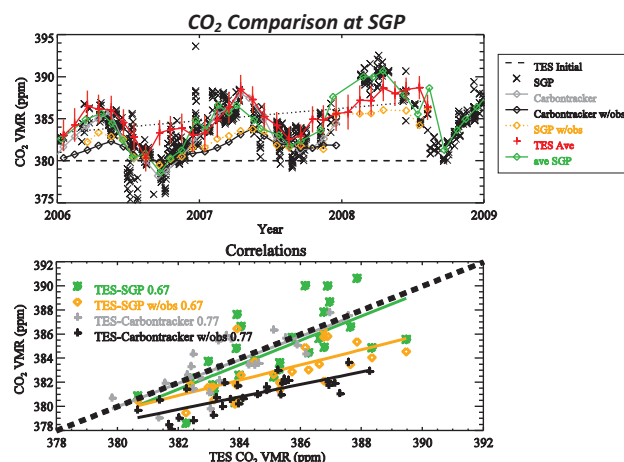
Fig. 12. Monthly averaged TES (~5 km, red), SGP aircraft data (2–7 km, green), and Carbontracker (black). SGP with the observation operator (orange) is influenced by the surface data and affected by seasonal variations in sensitivity. TES compared with SGP with the TES observation operator applied shows a high bias.

cycle somewhat similar to CarbonTracker, although averaging about ~1.5 ppm higher. The validation in the Southern Hemisphere relies on data at the surface and 10 km, with no validation data in the mid troposphere, so it is not possible to fully validate the TES Southern Hemisphere results.

6.4 Comparison to SGP aircraft data

Figure 12 shows comparisons to aircraft data from the SGP ARM site. Surface air at the SGP shows a seasonal drawdown arising from winter-wheat (April–May) and photosynthesis of more distant summer crops and grass (June–July) (Fischer et al., 2007; Riley et al., 2009). The aircraft data from 2–4 km and 4–7 km show very similar seasonal patterns at this location so aircraft data between 2–7 km were averaged monthly and compared to monthly averages of TES over the spatial region described in Fig. 3. Figure 12 shows the comparison of these data from 2006–2008, and the lower panel shows a correlation of 0.67 between TES and SGP aircraft data and 0.77 correlation between TES and Carbontracker. These correlations do not change when the TES observation operator is applied, however TES shows a high bias when the observation operator is applied, indicating more work is needed on the characterization of the TES bias correction. Since SGP is at one location with a few measurements per month and TES is averaging over most of the United States, it is not surprising that there are some differences between these measurements, however the differences are larger than expected. Comparisons of aircraft data from Sinton, Texas (at 4.5 km) and Beaver Crossing, Nebraska (at 5 km) to the SGP aircraft data above 2 km show differences of 1–2 ppm which indicate that TES land retrievals of CO_2 need improvement; one possible explanation that is now

Table 3. TES correlation to GLOBALVIEW, CarbonTracker, and AIRS for different subsets.

	Correlation GLOBALVIEW	Correlation CarbonTracker	Correlation AIRS	GLOBALVIEW station locations used for comparison
N. Hemisphere ocean	0.69	0.69	0.53	BME BMW CHR GMI HAA IZO KEY KUM MID MLO MNM RPB RYO YON GSN AZR PTA TAP
S. Hemisphere ocean	0.11	0.57	0.16	ASC CPT EIC SEY SMO RTA
Ocean	0.60	0.67	0.46	ASC BKT BME BMW CHR CPT EIC GMI HAA IZO KEY KUM MID MLO MNM RPB RYO SEY SMO YON GSN AZR PTA RTA TAP
Ocean altitude >2 km	0.83	0.74	0.56	MLO IZO
Land	0.16	0.36	0.24	ASK CFA MKN PTA SGP TAP TGC UTA WIS WKT WLG CPT GSN BKT
N. Hemisphere Land	0.35	0.52	0.48	ASK GSN PTA SGP TAP TGC UTA WIS WKT WLG
Land Altitude >2 km	0.51	0.24	0.28	ASK MKN WLG

Correlations of TES, GLOBALVIEW, CarbonTracker (at 500 hPa with TES observation operator applied), and AIRS (∼300 hPa) at subsets of GLOBALVIEW locations. Correlations are higher for ocean versus land, for northern versus Southern Hemisphere; and for higher versus lower altitude surface stations. The highest correlation is for ocean locations with altitude >2 km. Overall, TES correlates best with CarbonTracker.

being investigated is interference from emissivity due to a prominant silicate feature in the right laser band.

The correlations between TES and SGP are significantly lower than that obtained between TES and Mauna Loa or CONTRAIL data in the Northern Hemisphere. The lower correlation could indicate a problem in TES results over land, or could result because TES is averaging over a much of the US. Land data present more challenges than ocean, namely an uncertain and variable surface emissivity, and a less certain and more variable surface temperature. It is likely that the less optimal comparison with validation data is a combination of more interference of surface characteristics and more variable CO_2. This dataset is and will be useful for testing improvements to the TES retrieval algorithm.

### 6.5 Comparison to GLOBALVIEW and surface flasks

Comparisons of TES to GLOBALVIEW data are useful for a statistical validation of TES even though GLOBALVIEW mainly consists of surface site estimates and TES sensitivity peaks in the mid-troposphere. Processed TES data from January 2006 through September 2007 are compared to GLOBALVIEW surface values between 35° S and 40° N which includes 24 ocean and 14 land stations. We compare monthly averaged TES values which have at least 20 TES measurements within 830 km of the site in a month (resulting in about a 15° diameter circle centered at the site). Comparison of TES to GLOBALVIEW versus flasks yielded nearly identical results, with comparisons within 0.02 correlation of each other, so for simplicity only results compared to GLOBALVIEW are shown. Use of GLOBALVIEW data points

with a relative weight of at least 2 ("derived directly from the actual measurements") resulted in only 4 stations with not much improvement in statistics over using all weights, so all weights are used for comparisons.

Table 3 shows TES and GLOBALVIEW correlations for different subsets of locations; we find that ocean sites have significantly higher correlation than land locations, and that the Northern Hemisphere sites have significantly higher correlation than those in the Southern Hemisphere. We also find that high altitude sites (>2 km) correlate better with TES than lower altitude sites, likely because at high altitudes the measurement is made closer to the altitude of TES peak sensitivity. As shown in Table 4, offsetting TES ocean targets from GLOBALVIEW by latitude, longitude, or time resulted in a significant reduction in correlation between TES and GLOBALVIEW, validating patterns seen by TES in latitude, longitude, and time.

The mean difference between TES and GLOBALVIEW is 0.1 ppm (TES high) with the bias correction discussed in Sect. 5.5. The expected difference given in Stephens et al. (2007) for 4 km – surface values is −0.7 ppm. However, this bias fluctuates depending on which subset of data is used, so it indicates, but not conclusively, that the TES bias correction is too high. The predicted error for the TES averages (∼85 targets per month per GLOBALVIEW site) is 1.9 ppm. A scatter plot of TES versus GLOBALVIEW is shown in Fig. 13, which shows definite skill for TES, especially considering that the TES initial guess and a priori are both set to 380 ppm. The correlation is 0.60 and, as discussed above, decreases if TES is offset from GLOBALVIEW by time, latitude, or longitude.
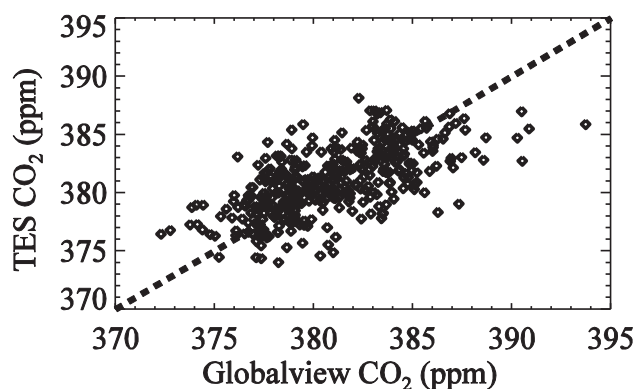
Fig. 13. TES versus GLOBALVIEW data for TES observations within 550 km of GLOBALVIEW sites. The agreement is significant given that TES starts with a uniform 380 ppm prior and initial guess.

Table 4. TES correlation to GLOBALVIEW at and offset from GLOBALVIEW locations.

	Time (± 1 month)	Latitude ($\pm 15°$)	Longitude ($\pm 30°$)
TES + shift	0.56	0.54	0.47
Aligned	0.60	0.60	0.60
TES − shift	0.44	0.44	0.52

This table shows correlation of TES shifted by the indicated amount versus GLOBALVIEW. This shows that TES agrees best with GLOBALVIEW when aligned to the same time, latitude, and longitude. This is for yearly de-trended data.

6.6 Comparison to CarbonTracker

TES is compared to CarbonTracker at the surface and at 500 hPa at GLOBALVIEW ocean locations. Because CarbonTracker spans the surface through 0.1 hPa, the TES observation operator can be applied to CarbonTracker for comparisons to TES. CarbonTracker is interpolated to the TES standard pressure grid (~65 levels from the surface through 0.1 hPa), the observation operator is applied on the TES standard pressure grid using Eq. (7), and the resultant value is sampled at 511 hPa for comparison to the TES results. For comparisons at the same ocean GLOBALVIEW sites as above, the correlations are 0.62 for TES versus CarbonTracker at the surface and 0.67 for TES versus CarbonTracker with the TES observation operator at 500 hPa, indicating a better agreement between TES and CarbonTracker when CarbonTracker is sampled at the TES pressure level. CarbonTracker at 500 hPa shows about 25% less seasonal variability than TES, and CarbonTracker with the TES observation operator shows about half the variability of TES in the Northern Hemisphere, as seen in Table 6 and illustrated in Fig. 11. TES is also compared to CarbonTracker at an offset from GLOBALVIEW locations by $\pm 15°$ latitude or

Table 5. TES and CarbonTracker correlations at and offset from GLOBALVIEW locations.

	−30 longitude	0	+30 longitude
+15 latitude		0.61	
0	0.57	0.67	0.58
−15 latitude		0.59	

Correlations of TES and CarbonTracker w/obs at 500 hPa at and offset from GLOBALVIEW locations for ocean scenes. This suggests that CarbonTracker agrees somewhat better with TES data at GLOBALVIEW locations. Both datasets de-trended by a 2 ppm/year increase.

Table 6. Variability and mean differences of monthly average data.

	OCEAN		LAND	
	Stdev (ppm)	Diff vs. TES (ppm)	Stdev (ppm)	Diff vs. TES (ppm)
GLOBALVIEW	3.3	0.1	4.3	0.7
CarbonTracker-surface	3.2	−0.8	4.2	−1.4
CarbonTracker 500 hPa	1.5	0.9	2.4	4.0
CarbonTracker 500 hPa w/obs	1.3	1.0	1.1	3.4
TES (511 hPa)	2.4	–	2.7	–
AIRS (~300 hPa)	1.5	0.9	1.6	2.4

Column 1 is the variability of each dataset and column 2 is the mean of (TES minus <dataset>) for data 1/2006 through 9/2007 with all data de-trended at a constant rate of 2 ppm per year. The first two columns are for GLOBALVIEW ocean locations and the last two are for land locations. TES has a positive bias compared to GLOBALVIEW and CarbonTracker at 500 hPa, but a negative bias compared to CarbonTracker at the surface. TES shows less variability than GLOBALVIEW and CarbonTracker at the surface, but more variability than CarbonTracker at 500 hPa, especially comparing to CarbonTracker with TES observation operator (w/obs).

$\pm 30°$ longitude in Table 5. TES and CarbonTracker correlate ~0.05 better at GLOBALVIEW locations compared to non-GLOBALVIEW locations. Overall TES compares better to CarbonTracker than to surface sites or AIRS.

6.7 Comparison to AIRS

We compare to the Chahine et al. (2005, 2008) AIRS CO_2 product, which is gridded ($2° \times 2.5°$) monthly data with peak sensitivity at 300 hPa (Olsen, 2009). As seen in Table 3, the correlation between TES and AIRS ranges between 0.16 for Southern Hemisphere ocean (which has a weak seasonal cycle) to 0.53 for Northern Hemisphere ocean, with AIRS seasonal variability less than TES, as seen in Table 6 and Fig. 11.

6.8 Spatial maps from TES, CarbonTracker, GLOBALVIEW, and AIRS

Maps of $15° \times 15°$ degree monthly-averaged TES data between 40° S and 45° N are shown for February, April, and
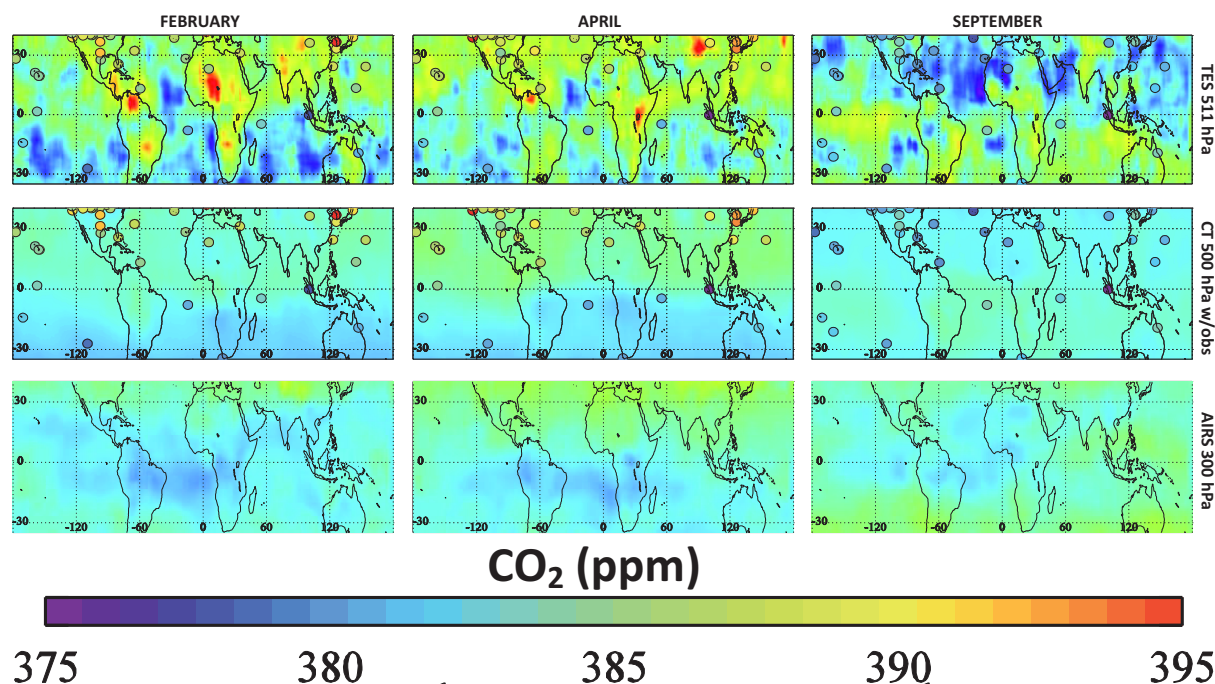
Fig. 14. TES (top), CarbonTracker at 500 hPa with the TES observation operator (middle), and AIRS (bottom) for February, April, and September, 2007. The small circles show values for $15° \times 15°$ monthly averages of TES and CarbonTracker sampled at the TES observation locations with the background color showing interpolation between these points. The AIRS data are shown as $2° \times 2.5°$ monthly averages. The large circles show GLOBALVIEW surface values. Some enhancements over land seen in TES are also seen in CarbonTracker data near the surface. In general TES exhibits more variability than CarbonTracker at 500 hPa. AIRS, TES, and CarbonTracker all show high values in the Northern Hemisphere in April, as expected, and the reverse in September. All color scales are the same.

September 2006 (with interpolation) in Fig. 14, with locations and values for GLOBALVIEW surface measurements overplotted (circles). For comparison purposes, Carbon-Tracker (at the surface and 500 hPa) is sampled at TES observation locations and monthly averaged on the same $15°$ grid. The 500 hPa value shows the CarbonTracker profile mapped to the TES 5 retrieval values, and sampled at 511 hPa. Surface values from CarbonTracker are also shown, which show some correlation with the high values seen by TES over land in Africa, South America, and Asia, suggesting more vertical transport in these locations than included in CarbonTracker. AIRS on a monthly $2° \times 2.5°$ grid is also shown. High CO_2 values are seen in TES, Carbon-Tracker, and AIRS data for April 2007 in the Northern Hemisphere, as expected. September/October is the seasonal minimum of CO_2 in the Northern Hemisphere, and lower values are seen in all 3 datasets in the Northern Hemisphere. In general, TES shows more longitudinal variability than Car-bonTracker. Correlations between TES and GLOBALVIEW suggest the longitudinal variations seen by TES are meaningful (see Table 4).

7 Investigating the potential of TES CO_2 in for inverse modeling

We conducted an OSSE to assess the potential utility of the TES data for inverse modeling of CO_2 fluxes. As discussed in Sect. 1, several studies have suggested that satellite observations of CO_2 when averaged on spatial scales of $8° \times 10°$, for example, and on weekly or monthly timescales can provide valuable new constraints on estimates of CO_2 fluxes if the precision of the data is better than about 2.5 ppm. We examine here the reduction in uncertainty of CO_2 flux estimates obtained when simulated unbiased TES data are averaged monthly on spatial scales of $10° \times 10°$, $15° \times 15°$ and $20° \times 30°$.

7.1 Inversion configuration

7.1.1 Forward model

We use the GEOS-Chem global chemical transport model (CTM) to simulate a pseudo-atmosphere from which pseudo-observations of CO_2 from TES are generated. The GEOS-Chem model uses meteorological fields from the NASA Global Modeling and Assimilation Office (GMAO). We use version v8-01-01 with GEOS-4 meteorological fields at a

5616 S. S. Kulawik et al.: Characterization of TES CO$_2$ for carbon cycle science
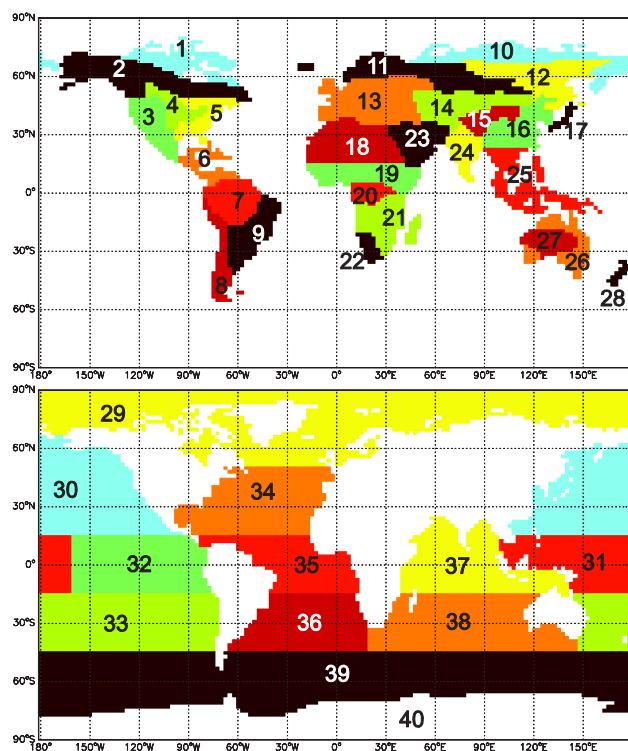
Fig. 15. The 40 regions used in our inversions are defined as the standard 11 TransCom 3 ocean regions, 28 land regions based on AVHRR definitions of dominant vegetative types, and the Rest of the World (ROW) consisting of mostly Antarctic/Greenland and some small isolated islands. Coastal grid boxes can belong to both land and ocean regions.

horizontal resolution of 2°×2.5° and with 30 vertical sigma levels. The model has multiple separate simulation modes, the most common of which is the O$_x$-NO$_x$-hydrocarbon chemistry mode (Bey et al., 2001). The CO$_2$ simulation mode run for this work contains no chemistry, but accounts for CO$_2$ emissions and uptake at the land and marine surface from both anthropogenic and natural sources. The original version of the CO$_2$ simulation is described in Suntharalingam et al. (2003, 2004) but significant improvements have been implemented in conjunction with this work, as described in Nassar et al. (2010).

7.1.2 Inversion methodology

We examine the potential of the TES data to reduce uncertainty in estimates of CO$_2$ fluxes from the 28 land and 11 ocean regions shown in Fig. 15. The ocean regions are the standard TransCom 3 ocean regions (Baker et al., 2006), whereas the land is spatially divided based on AVHRR dominant vegetation types (Hansen et al., 1998, 2000) to obtain the given regions, as described in Nassar et al. (2010). One additional tracer for the Rest of World (ROW) is used to

aggregate fluxes from areas not included in any other region, such as Greenland/Antarctic or small isolated islands.

In our inversion approach, the fluxes used to generate the pseudo-data are defined as the "truth." We then use the pseudo-data to sequentially update and thus optimize the flux estimates, starting from an a priori estimate of the fluxes that is different from the truth. We use the maximum a posteriori (MAP) approach described in Jones et al. (2003, 2009), in which we minimize the following cost function

$$\mathbf{J}(\boldsymbol{u}) = (\hat{\boldsymbol{x}} - \mathbf{F}(\boldsymbol{u}))^T \mathbf{S}_\epsilon (\hat{\boldsymbol{x}} - \mathbf{F}(\boldsymbol{u})) \tag{9}$$
$$+ (\boldsymbol{u} - \boldsymbol{u}_a)^T \mathbf{S}_a^{-1} (\boldsymbol{u} - \boldsymbol{u}_a)$$

where $\hat{\boldsymbol{x}}$ is the observation vector that consists of the TES CO$_2$ retrievals at the 511 hPa level, $\boldsymbol{u}$ is the state vector with elements representing the CO$_2$ flux from each region, $\boldsymbol{u}_a$ is the a priori state vector, $\mathbf{S}_\epsilon$ is the TES observation error covariance matrix, and $\mathbf{S}_a$ is the a priori covariance matrix for the fluxes. $\mathbf{F}(\boldsymbol{u})$ is the forward model which reflects the transport of the CO$_2$ fluxes in the GEOS-Chem model and the TES observation operator (which accounts for the TES sensitivity and a priori profile as described in Sect. 3.3.2). Both the TES retrieval $\hat{\boldsymbol{x}}$ and the forward model simulation of the observations are expressed with respect to the natural logarithm of the CO$_2$ volume mixing ratio (VMR). The expression for $\mathbf{F}(\boldsymbol{u})$ is analogous to Eq. (7)

$$\mathbf{F}(\boldsymbol{u}) = \boldsymbol{x}_a + \mathbf{A}(\ln[\mathbf{H}(\boldsymbol{u})] - \boldsymbol{x}_a) \tag{10}$$

where $\mathbf{H}(\boldsymbol{u})$ is the modeled CO$_2$ profile interpolated onto the TES retrieval grid, $\boldsymbol{x}_a$ is the TES a priori (given in terms of the logarithm of the CO$_2$ mixing ratio), and $\mathbf{A}$ is the TES averaging kernel. To minimize possible representation errors in the spatio-temporal averaging of the pseudo-data and the model, the model is first sampled at the location and time (to within 1 h) of each TES global survey observation and then averaged monthly and spatially in bins of 10°×10°, 15°×15°, or 20°×30°. We generate pseudo-data for 2006 and ingest the monthly mean pseudo-data over the entire year to obtain an annual mean estimate of the fluxes.

7.2 Inversion results

The results of the inversion analysis are given in Table 7 and Fig. 16. Shown are the ratio of the optimized flux estimates to the truth and the ratio of the a posteriori to a priori uncertainties for the 40 flux regions and for the three different bin sizes used for averaging the TES data. The differences between the inversions with the different bin sizes are not large. All three inversions indicate that the TES data provide the most constraints on estimates of the tropical fluxes. All three datasets produced the largest error reduction on fluxes from the Southern African Grasslands and the South American Tropical Rain Forest; the ratio of the a posteriori to a priori uncertainty was 0.27 for fluxes from these two regions with the 10°×10° data.
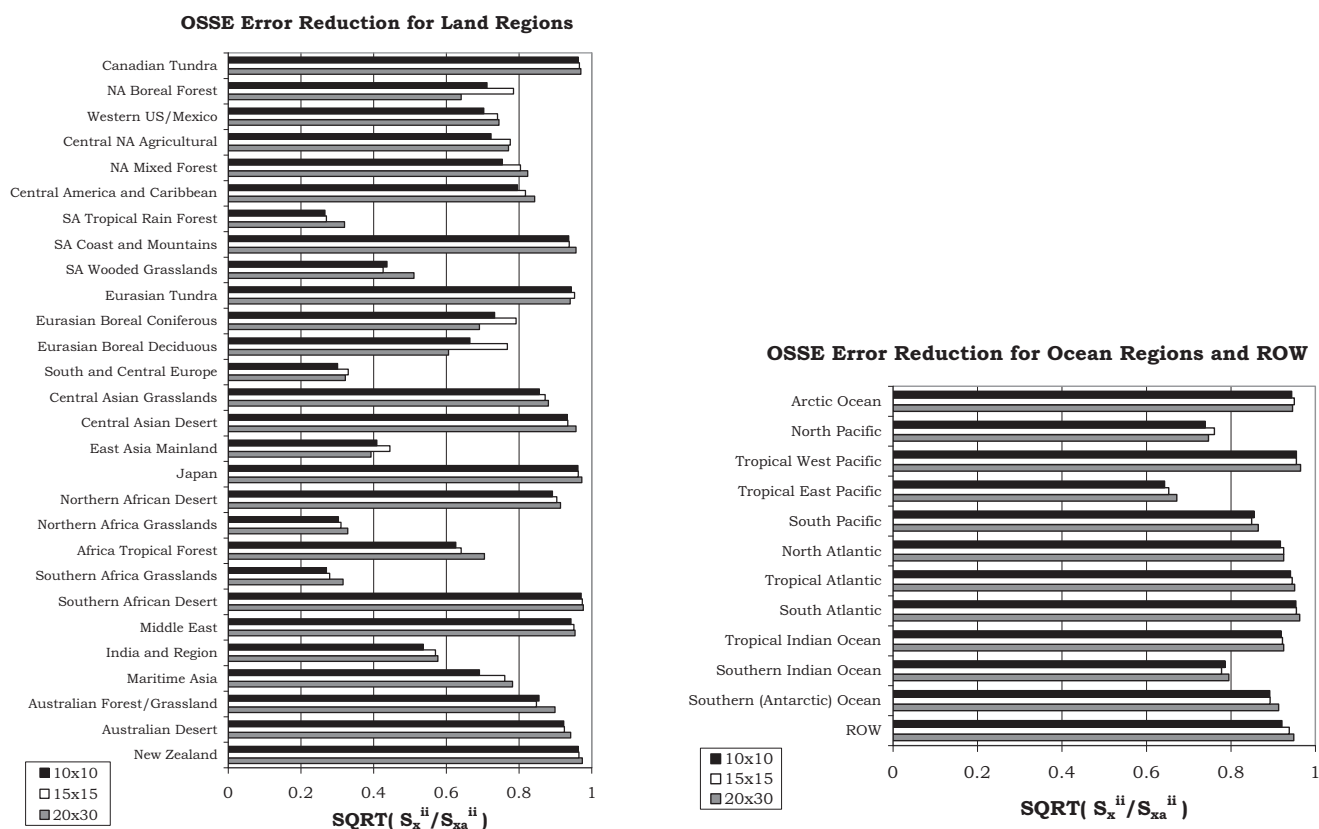
Fig. 16. OSSE uncertainty ratios for the land, ocean and ROW regions at 3 different resolutions ($10° \times 10°$, $15° \times 15°$ and $20° \times 30°$). Lower ratios indicate a larger error reduction.

Examination of the uncertainty reduction (the difference between unity and the ratio of the a posteriori to a priori uncertainties) across all the regions indicates that the TES data provide the largest error reduction on the fluxes when averaged on $10° \times 10°$ scales. At $10° \times 10°$, 6 regions gave an error ratio less than 0.50, compared to 5 regions with the $20° \times 30°$ data. These regions are South American Tropical Rain Forest, Southern Africa Grasslands, South and Central Europe, Northern Africa Grasslands, East Asia Mainland, and South American Wooded Grasslands.

The trace of the inversion resolution matrix is an indication of the number of regions in the 40-element state vector which are constrained independently in the inversion. This is analogous to the DOFs for a profile retrieval. The traces obtained with the $10° \times 10°$, $15° \times 15°$, and $20° \times 30°$ data were 14.9, 13.9, and 13.7. We found that at $20° \times 30°$ the data provide greater error reduction on the boreal fluxes, whereas the $10° \times 10°$ data offered more constraints on the mid-latitude and tropical fluxes.

The greater uncertainty reduction obtained with the $10° \times 10°$ averaging is somewhat expected since the monthly mean observation error of the TES data increases from about 1 ppm at $20° \times 30°$ to 2 ppm at $10° \times 10°$, whereas the amount of data ingested in the inversion analysis increases by a factor

of 6 at $10° \times 10°$. Interestingly, although the $15° \times 15°$ averaging (which has a monthly mean observation error of about 1.4 ppm) produced only a modest increase in the DOFs (13.9 compared to 13.7 at $20° \times 30°$), it gives an a posteriori estimate of the fluxes that is closest to the truth. With the $15° \times 15°$ averaging there are 19 elements of the 40-element state vector with the smallest residual error, compared to 12 with the $10° \times 10°$ data and 9 with the $20° \times 30°$ data.

The results presented here suggest that TES CO$_2$ have the potential to provide additional information on the CO$_2$ fluxes. However, it is important to recognize that ability of the OSSE to reliably constrain the true flux estimates reflects the fact that both the model and the pseudo-data were unbiased in the OSSE. If biases in the model and the real data are not properly characterized and accounted for, the inferred flux estimates in the inversion analysis will be biased. Furthermore, although averaging the data reduces the random errors in the measurement, which improves the measurement precision, it could lead to a loss of information associated with atmospheric processes on spatial and temporal scales smaller than that on which the averaging is done. An alternative would be to exploit the individual retrievals without averaging. On the other hand, the large random error in the individual measurements could be an issue for inverse modeling.

Table 7. OSSE a posteriori flux estimates compared with the "true" state along with a ratio of the a posteriori error relative to the a priori error for 40 geographic regions. The shaded regions, primarily in the tropics, show regions with the most information added from TES.

		X_{true}	X_{post}/X_{true}			Predicted a posteriori error/ a priori error		
	FLUX REGIONS	TgC/yr	10×10	15×15	20×30	10×10	15×15	20×30
1	North American Tundra	27.2	1.04	1.00	1.04	0.96	0.97	0.97
2	North American Boreal Forest	−35.2	1.05	0.89	0.63	0.71	0.79	0.64
3	Western US and Mexico	−459.3	0.58	1.08	1.15	0.70	0.74	0.75
4	Central North America	−298.5	0.92	1.11	1.07	0.72	0.78	0.77
5	North American Mixed Forest	−270.8	1.18	0.87	1.20	0.75	0.80	0.82
6	Central America and Caribbean	164.1	0.85	1.01	1.28	0.80	0.82	0.84
7	South American Tropical Rain Forest	494.0	1.03	0.95	0.94	0.27	0.27	0.32
8	South American Coast and Mountains	−190.5	1.10	1.03	1.15	0.94	0.94	0.96
9	South American Wooded Grasslands	−470.9	0.96	1.25	1.26	0.44	0.43	0.51
10	Eurasian Tundra	−167.6	1.17	1.04	0.96	0.94	0.95	0.94
11	Eurasian Boreal Coniferous	−388.0	1.01	1.05	0.94	0.73	0.79	0.69
12	Eurasian Boreal Deciduous	−215.0	0.94	0.88	1.01	0.67	0.77	0.61
13	South and Central Europe	−664.1	1.15	0.91	0.88	0.30	0.33	0.32
14	Central Asian Grasslands	−138.0	0.92	1.03	1.16	0.86	0.87	0.88
15	Central Asian Desert	−39.3	0.93	1.01	1.01	0.93	0.93	0.96
16	East Asian Mainland	−87.6	1.10	1.03	1.02	0.41	0.45	0.39
17	Japan	−4.8	1.06	1.03	0.93	0.96	0.96	0.97
18	Northern African Desert	−69.4	1.08	1.02	0.97	0.89	0.90	0.91
19	Northern African Grasslands	−80.7	0.98	1.30	0.85	0.30	0.31	0.33
20	African Tropical Forest	−249.9	0.87	0.94	1.08	0.63	0.64	0.71
21	Southern Africa Grasslands	−792.4	1.02	0.95	0.74	0.27	0.28	0.32
22	Southern African Desert	−109.6	0.97	0.99	1.07	0.97	0.97	0.98
23	Middle East	−70.6	1.16	1.01	1.08	0.94	0.95	0.95
24	India and Region	−44.6	1.18	0.70	1.03	0.54	0.57	0.58
25	Maritime Asia	−61.9	1.25	0.93	1.04	0.69	0.76	0.78
26	Australian Forest/Grassland	−112.3	0.90	1.15	1.15	0.86	0.85	0.90
27	Australian Desert	−108.8	1.13	0.86	1.17	0.92	0.93	0.94
28	New Zealand	−6.9	1.02	1.04	1.08	0.96	0.97	0.97
29	Arctic Ocean	−278.3	1.02	1.09	0.98	0.94	0.95	0.95
30	North Pacific	−504.4	1.01	1.03	0.91	0.74	0.76	0.75
31	Tropical West Pacific	50.2	0.97	0.93	1.00	0.96	0.96	0.97
32	Tropical East Pacific	427.4	1.12	1.12	1.00	0.64	0.65	0.67
33	South Pacific	−326.7	1.20	0.88	0.92	0.86	0.85	0.87
34	North Atlantic	−01.2	0.90	1.02	0.96	0.92	0.93	0.93
35	Tropical Atlantic	114.0	1.17	0.96	0.93	0.94	0.95	0.95
36	South Atlantic	−157.7	0.96	1.01	1.17	0.95	0.96	0.96
37	Tropical Indian Ocean	114.2	1.07	1.00	1.05	0.92	0.92	0.93
38	Southern Indian Ocean	−442.9	0.93	0.90	1.11	0.79	0.78	0.80
39	Southern Ocean	−181.6	1.05	0.90	0.86	0.89	0.89	0.91
40	Rest of the World (ROW)	−40.1	1.08	1.09	1.12	0.92	0.94	0.95

For example, Wang et al. (2009) showed that a joint inversion analysis of CO and CO$_2$, exploiting the correlations in the model errors for CO and CO$_2$ would provide more constraints on the CO$_2$ fluxes than using only CO$_2$. But a requirement of joint inversion approach, as noted by Wang et al. (2009), is that the measurement error must be smaller than the model error. A more detailed analysis is clearly needed to better assess the potential impact of the spatial and temporal averaging of the data on the inferred flux estimates.

8 Conclusions

Carbon dioxide retrievals from the TES instrument between 40° S and 45° N over 3 years are shown in comparison to surface data, SGP and CONTRAIL aircraft data, satellite data from AIRS and to assimilated data from CarbonTracker. The peak TES sensitivity is at 511 hPa (∼5 km), with about 10% of the sensitivity in the lower troposphere and about 1 degree of freedom total. We find a low bias of 2.1% in TES CO_2 which has been corrected using Mauna Loa data at 3.4 km altitude, however the bias correction would be more accurately quantified by comparisons to profile aircraft data at a well-mixed location with values from the surface through ∼11 km to cover the range of TES sensitivity. Maps of TES CO_2 show expected latitudinal gradients and seasonal features, with more longitudinal features than seen in CarbonTracker. The characterization of TES sensitivity and errors shows that for the monthly-averaged TES there is good agreement between the predicted and actual sensitivity and errors, with errors decreasing as predicted as more profiles are averaged. The monthly predicted error for a 15°×15° average (with ∼80 targets per bin) between 40° S and 45° N is 2.2 ppm.

The CO_2 abundances from TES, Mauna Loa, CON-TRAIL, AIRS, and CarbonTracker in the northern tropical Pacific all show similar seasonal cycles. TES correlates best with the Mauna Loa data, which are collected at 3.4 km, comparable the location of the peak TES sensitivity, near 5 km. In the southern Pacific, although all datasets show a yearly increase in CO_2, the correlation of TES to the other datasets is much smaller. Comparisons of TES monthly averages to SGP aircraft data over the US show a correlation of about 0.7, which is significantly less than over the ocean in the Northern Hemisphere due to a combination of more variability over land (as TES is averaged over a large area) and greater challenges for land retrievals.

At 39 GLOBALVIEW sites, TES is compared to Carbon-Tracker, AIRS, and GLOBALVIEW. Comparison of TES to GLOBALVIEW surface sites shows a 0.60 correlation at ocean sites and a 0.16 correlation at land sites, with low correlation over land likely related to the sharp gradients seen over land between the surface and free troposphere. Although the troposphere is not expected to completely correlate with the surface, it is significant that the correlations between TES and GLOBALVIEW decrease if the TES data are shifted in latitude, longitude, or time compared to GLOBALVIEW. TES correlates best with CarbonTracker (at 500 hPa with the TES observation operator applied), yielding a 0.67 correlation at ocean sites and 0.36 correlation at land sites. Comparing the variability of the CO_2 data at ocean sites shows that TES variability (2.4 ppm) is less than the surface data (3.3 ppm), but significantly more than Carbon-Tracker (w/obs) (1.3 ppm) or AIRS (1.5 ppm).

An OSSE using simulated TES observations based on GEOS-Chem model output shows that TES data can reduce uncertainty in regional CO_2 fluxes when the data are averaged monthly and on various spatial scales. TES data averaged at 10°×10°, for example, have a total error of about 2.4 ppm and produced a large reduction (of about 70%) in uncertainty of estimates of CO_2 fluxes from tropical land regions, such as the South American Tropical Rain Forests, Southern African Grasslands, Northern African Grasslands, as well as Southern and Central Europe. Many of these regions are areas where GLOBALVIEW coverage is relatively sparse. Our results suggests that if biases in the TES CO_2 data and the model are properly characterized and accounted for, the data will provide sufficient information to reliably quantify CO_2 sources and sinks. Since the TES sensitivity peaks in the middle troposphere, the instrument should offer complementary information to the surface data and, therefore, integrating TES with the surface data should offer valuable new constraints for inverse modeling of carbon fluxes.

References

Baker, D. F., Law, R. M., Gurney, K. R., Rayner, P., Peylin, P., Denning, A. S., Bousquet, P., Bruhwiler, L., Chen, Y. H., Ciais, P., Fung, I. Y., Heimann, M., John, J., Maki, T., Maksyutov, S., Masarie, K., Prather, M., Pak, B., Taguchi, S., and Zhu, Z.: TransCom 3 inversion intercomparison: Impact of transport model errors on the interannual variability of regional CO$_2$ fluxes, 1988–2003, Global Biogeochem. Cy., 20(1), GB1002, doi:10.1029/2004GB002439, 2006.

Barkley, M. P., Frieß, U., and Monks, P. S.: Measuring atmospheric CO$_2$ from space using Full Spectral Initiation (FSI) WFM-DOAS, Atmos. Chem. Phys., 6, 3517–3534, doi:10.5194/acp-6-3517-2006, 2006.

Beer, R. TES on the Aura mission: Scientific objectives, measurements, and analysis overview, IEEE T. Geosci. Remote, 44(5), 1102–1105, 2006.

Bey, I., Jacob, D. J., Yantosca, R. M., Logan, J. A., Field, B. D., Fiore, A. M., Li, Q. B., Liu, H. G. Y., Mickley, L. J., and Schultz, M. G.: Global modeling of tropospheric chemistry with assimilated meteorology: Model description and evaluation, J. Geophys. Res.-Atmos., 106(D19), 23073–23095, 2001.

Bösch, H., Toon, G. C., Sen, B., Washenfelder, R. A., Wennberg, P. O., Buchwitz, M., de Beek, R., Burrows, J. P., Crisp, D., Christi, M., Connor, B. J., Natraj, V., and Yung, Y. L.: Space-based near-infrared CO$_2$ measurements: Testing the Orbiting Carbon Observatory retrieval algorithm and validation concept using SCIA-MACHY observations over Park Falls, Wisconsin, J. Geophys. Res.-Atmos., 111(D23), doi:10.1029/2006JD007080, 2006.

Bowman, K. W., Rodgers, C. D., Kulawik, S. S., Worden, J., Sarkissian, E., Osterman, G., Steck, T., Lou, M., Eldering, A., Shephard, M., Worden, H., Lampel, M., Clough, S., Brown, P., Rinsland, C., Gunson, M., and Beer, R.: Tropospheric emission spectrometer: Retrieval method and error analysis, IEEE T. Geosci. Remote, 44(5), 1297–1307, 2006.

Buchwitz, M., de Beek, R., Burrows, J. P., Bovensmann, H., Warneke, T., Notholt, J., Meirink, J. F., Goede, A. P. H., Bergamaschi, P., Körner, S., Heimann, M., and Schulz, A.: Atmospheric methane and carbon dioxide from SCIAMACHY satellite data: initial comparison with chemistry and transport models, Atmos. Chem. Phys., 5, 941–962, doi:10.5194/acp-5-941-2005, 2005.

Buchwitz, M., Schneising, O., Burrows, J. P., Bovensmann, H., Reuter, M., and Notholt, J.: First direct observation of the atmospheric CO$_2$ year-to-year increase from space, Atmos. Chem. Phys., 7, 4249–4256, doi:10.5194/acp-7-4249-2007, 2007.

Chahine, M., Barnet, C., Olsen, E. T., Chen, L., and Maddy, E.: On the determination of atmospheric minor gases by the method of vanishing partial derivatives with application to CO$_2$, Geophys. Res. Lett., 32(22), doi:10.1029/2005GL024165, 2005.

Chahine, M. T., Chen, L., Dimotakis, P., Jiang, X., Li, Q. B., Olsen, E. T., Pagano, T., Randerson, J., and Yung, Y. L.: Satellite remote sounding of mid-tropospheric CO$_2$, Geophys. Res. Lett., 35(17), doi:10.1029/2008GL035022, 2008.

Chevallier, F., Engelen, R. J., and Peylin, P.: The contribution of AIRS data to the estimation of CO$_2$ sources and sinks, Geophys. Res. Lett., 32(23), L23801, doi:10.1029/2005GL024229, 2005.

Chevallier, F., Engelen, R. J., Carouge, C., Conway, T. J., Peylin, P., Pickett-Heaps, C., Ramonet, M., Rayner, P. J., and Xueref-Remy, I.: AIRS-based versus flask-based estimation of carbon surface fluxes, J. Geophys. Res.-Atmos., 114, D20303, doi:10.1029/2009JD012311, 2009.

Conway, T. J., Lang, P. M., and Masarie, K. A.: Atmospheric Carbon Dioxide Dry Air Mole Fractions from the NOAA ESRL Carbon Cycle Cooperative Global Air Sampling Network, 1968–2007, Version: 2008-07-24, Path: ftp://ftp.cmdl.noaa.gov/ccg/co2/flask/event/, last access: August 2009, 2008.

Crevoisier, C., Chedin, A., and Scott, N. A.: AIRS channel selection for CO$_2$ and other trace-gas retrievals, Q. J. Roy. Meteorol. Soc., 129(593), 2719–2740, 2003.

Crevoisier, C., Chédin, A., Matsueda, H., Machida, T., Armante, R., and Scott, N. A.: First year of upper tropospheric integrated content of CO$_2$ from IASI hyperspectral infrared observations, Atmos. Chem. Phys., 9, 4797–4810, doi:10.5194/acp-9-4797-2009, 2009.

Crisp, D., Atlas, R. M., Breon, F.-M., Brown, L. R., Burrows, J. P., Ciais, P., Connor, B. J., Doney, S. C., Fung, I. Y., Jacob, D. J., Miller, C. E., O'Brien, D., Pawson, S., Randerson, J. T., Rayner, P., Salawitch, R. J., Sander, S. P., Sen, B., Stephens, G. L., Tans, P. P., Toon, G. C., Wennberg, P. O., Wofsy, S. C., Yung, Y. L., Kuang, Z., Chudasama, B., Sprague, G., Weiss, B., Pollock, R., Kenyon, D., and Schroll, S.: The Orbiting Carbon Observatory (OCO) mission, Adv. Space Res., 34(4), 700–709, 2004.

Dana, V., Mandin, J. Y., Guelachvili, G., Kou, Q., Morillonchapey, M., Wattson, R. B., and Rothman, L. S.: Intensities and Self-Broadening Coefficients of (CO$_2$)-C-12-O-16 Lines in the Laser Band Region, J. Mol. Spectrosc., 152(1), 328–341, 1992.

Devi, V. M., Benner, D. C., Smith, M. A. H., Brown, L. R., and Dulick, M.: Multispectrum analysis of pressure broadening and pressure shift coefficients in the (CO$_2$)-C-12-O-16 and (CO$_2$)-C-13-O-16 laser bands, J. Quant. Spectrosc. Ra., 76(3–4), 411–434, 2003.

Eldering, A., Kulawik, S. S., Worden, J., Bowman, K., and Osterman, G.: Implementation of cloud retrievals for TES atmospheric retrievals: 2. Characterization of cloud top pressure and effective optical depth retrievals, J. Geophys. Res.-Atmos., 113(D16), D16S37, doi:10.1029/2007JD008858, 2008.

Engelen, R. J. and Stephens, G. L.: Information content of infrared satellite sounding measurements with respect to CO$_2$, J. Appl. Meteorol., 43(1), 373–378, 2004.

Enting, I. G. and Mansbridge, J. V.: Latitudinal Distribution of Sources and Sinks of CO$_2$ – Results of an Inversion Study, Tellus B, 43(1), 156–170, 1991.

Feng, L., Palmer, P. I., Bösch, H., and Dance, S.: Estimating surface CO$_2$ fluxes from space-borne CO$_2$ dry air mole fraction observations using an ensemble Kalman Filter, Atmos. Chem. Phys., 9, 2619–2633, doi:10.5194/acp-9-2619-2009, 2009.

Fischer, M. L., Billesbach, D. P., Berry, J. A., Riley, W. J., and Torn, M. S.: Spatiotemporal variations in growing season exchanges of v, H$_2$O, and sensible heat in agricultural fields of the Southern Great Plains, Earth Interact., 11(17), 1-21, 2007.

GLOBALVIEW-CO$_2$: Cooperative Atmospheric Data Integration Project - Carbon Dioxide, CD-ROM, NOAA ESRL, Boulder, Colorado, also available on Internet via anonymous FTP to ftp.cmdl.noaa.gov, last access: July 2009, Path: ccg/co2/GLOBALVIEW, 2008.

Gloor, M., Fan, S. M., Pacala, S., and Sarmiento, J.: Optimal sampling of the atmosphere for purpose of inverse modeling: A model study, Global Biogeochem. Cy., 14(1), 407–428, 2000.

Hamazaki, T., Kuze, A., and Kondo, K.: Sensor system for Greenhouse Gas Observing Satellite (GOSAT), Proceedings of SPIE-The International Society for Optical Engineering 2004, vol. 5543, edited by: Barnes, W. L., Infrared Spaceborne Remote Sensing XII, Bellingham, WA, 275–282, 2004.

Hamazaki, T., Kuze, A., Team, G. P., and Agency, J. A. E.: CARBON DIOXIDE MONITORING FROM THE GOSAT SATELLITE, XXth ISPRS Congress, Istanbul, Turkey, 2004.

Hansen, M. C., Defries, R. S., Townshend, J. R. G., and Sohlberg, R.: UMD Global Land Cover Classification, 1×1 degree resolution, Department of Geography, University of Maryland, College Park, Maryland, 1981–1994, 1998.

Hansen, M. C., Defries, R. S., Townshend, J. R. G., and Sohlberg, R.: Global land cover classification at 1km spatial resolution using a classification tree approach, Int. J. Remote Sens., 21(6–7), 1331–1364, 2000.

Herman, R. L., Fisher, B. M., Shephard, M. W., Payne, V. H., Cady-Pereira, K. E., Kulawik, S. S., and Eldering, A.: Comparisons of Aura TES V004 Temperature Retrievals With Sonde Measurements, Eos Trans. AGU, 89(53), Fall Meet. Suppl., Abstract A53A-0251, 2008.

Houweling, S., Breon, F.-M., Aben, I., Rödenbeck, C., Gloor, M., Heimann, M., and Ciais, P.: Inverse modeling of CO$_2$ sources and sinks using satellite data: a synthetic inter-comparison of measurement techniques and their performance as a function of space and time, Atmos. Chem. Phys., 4, 523–538, doi:10.5194/acp-4-523-2004, 2004.

IPCC, 2007: Climate Change 2007: The Physical Science Basis, Contribution of Working Group I to the Fourth Assessment Report of the Intergovernmental Panel on Climate Change, edited by: Solomon, S., Qin, D., Manning, M., Chen, Z., Marquis, M., Averyt, K. B., Tignor, M., and Miller, H. L., Cambridge University Press, Cambridge, UK and New York, NY, USA, 2007.

Johns, J. W. C. and Vanderauwera, J.: Absolute Intensities in CO$_2$ – the V2 Fundamental near 15-Mu-M, J. Mol. Spectrosc., 140(1), 71–102, 1990.

Johns, J. W. C. and Noel, M.: Absolute Intensities in CO$_2$ – the Laser Bands near 10-Mu-M, J. Mol. Spectrosc., 156(1), 403–414, 1992.

Jones, D. B. A., Bowman, K. W., Palmer, P. I., Worden, J. R., Jacob, D. J., Hoffman, R. N., Bey, I., and Yantosca, R. M.: Potential of observations from the Tropospheric Emission Spectrometer to constrain continental sources of carbon monoxide, J. Geophys. Res.-Atmos., 108(D24), 4789, doi:10.1029/2003JD003702, 2003.

Jones, D. B. A., Bowman, K. W., Logan, J. A., Heald, C. L., Liu, J., Luo, M., Worden, J., and Drummond, J.: The zonal structure of tropical O$_3$ and CO as observed by the Tropospheric Emission Spectrometer in November 2004 - Part 1: Inverse modeling of CO emissions, Atmos. Chem. Phys., 9, 3547–3562, doi:10.5194/acp-9-3547-2009, 2009.

Kerola, D. X., Lampel, M. C., Shephard, M. W., Osterman, G. B., Herman, R. L., and Eldering, A.: Validation of Tropospheric Emission Spectrometer (TES) Sea Surface Temperature (SST) Retrievals, manuscript in preparation, 2010.

Kulawik, S. S., Osterman, G., Jones, D. B. A., and Bowman, K. W.: Calculation of altitude-dependent Tikhonov constraints for TES nadir retrievals, IEEE T. Geosci. Remote, 44(5), 1334–1342, 2006.

Kulawik, S. S., Bowman, K. W., Luo, M., Rodgers, C. D., and Jourdain, L.: Impact of nonlinearity on changing the a priori of trace gas profile estimates from the Tropospheric Emission Spectrometer (TES), Atmos. Chem. Phys., 8, 3081–3092, doi:10.5194/acp-8-3081-2008, 2008.

Le Quere, C., Rodenbeck, C., Buitenhuis, E. T., Conway, T. J., Langenfelds, R., Gomez, A., Labuschagne, C., Ramonet, M., Nakazawa, T., Metzl, N., Gillett, N., and Heimann, M.: Saturation 5 of the Southern Ocean CO$_2$ sink due to recent climate change, Science, 316, 1735-1738, 2007.

Luo, M., Rinsland, C., Fisher, B., Sachse, G., Diskin, G., Logan, J., Worden, H., Kulawik, S., Osterman, G., Eldering, A., Herman, R., and Shephard, M.: TES carbon monoxide validation with DACOM aircraft measurements during INTEX-B 2006, J. Geophys. Res.-Atmos., 112(D24), D24S48, doi:10.1029/2007JD008803, 2007.

Luo, M., Rinsland, C. P., Rodgers, C. D., Logan, J. A., Worden, H., Kulawik, S., Eldering, A., Goldman, A., Shephard, M. W., Gunson, M., and Lampel, M.: Comparison of carbon monoxide measurements by TES and MOPITT: Influence of a priori data and instrument characteristics on nadir atmospheric species retrievals, J. Geophys. Res.-Atmos., 112(D9), D09303, doi:10.1029/2006JD007663, 2007.

Machida, T., Matsueda, H., Sawa, Y., Nakagawa, Y., Hirotani, K., Kondo, N., Goto, K., Nakazawa, T., Ishikawa, K., and Ogawa, T.: Worldwide Measurements of Atmospheric CO$_2$ and Other Trace Gas Species Using Commercial Airlines, J. Atmos. Ocean. Tech., 25(10), 1744–1754, 2008.

Maddy, E. S., Barnet, C. D., Goldberg, M., Sweeney, C., and Liu, X.: CO$_2$ retrievals from the Atmospheric Infrared Sounder: Methodology and validation, J. Geophys. Res.-Atmos., 113(D11), D11301, doi:10.1029/2007JD009402, 2008.

Masarie, K. A. and Tans, P. P.: Extension and integration of atmospheric carbon dioxide data into a globally consistent measurement record, J. Geophys. Res.-Atmos, 100(D6), 11593–11610, 1995.

Matsueda, H., Inoue, H. Y., and Ishii, M.: Aircraft observation of carbon dioxide at 8–13 km altitude over the western Pacific from 1993 to 1999, Tellus B, 54(1), 1–21, 2002.

Matsueda, H., Machida, T., Sawa, Y., Nakagawa, Y., Hirotani, K., Ikeda, H., Kondo, N., and Goto, K.: Evaluation of atmospheric CO$_2$ measurements from new flask air sampling of JAL airliner observation, Pap. Meteorol. Geophys., 59, 1–17, 2008.

Nassar, R., Logan, J. A., Worden, H. M., Megretskaia, I. A., Bowman, K. W., Osterman, G. B., Thompson, A. M., Tarasick, D. W., Austin, S., Claude, H., Dubey, M. K., Hocking, W. K., Johnson, B. J., Joseph, E., Merrill, J., Morris, G. A., Newchurch, M., Oltmans, S. J., Posny, F., Schmidlin, F. J., Vomel, H., Whiteman, D. N., and Witte, J. C.: Validation of Tropospheric Emission Spectrometer (TES) nadir ozone profiles using ozonesonde measurements, J. Geophys. Res.-Atmos., 113(D15), D15S17, doi:10.1029/2007JD008819, 2008.

Nassar, R., Jones, D. B. A., Suntharalingam, P., Chen, J. M., Andres, R. J., Wecht, K. J., Yantosca, R. M., Kulawik, S. S., Bowman, K. W., Worden, J. R., Machida, T., and Matsueda, H.: Modeling global atmospheric CO_2 with improved emission inventories and CO_2 production from the oxidation of other carbon species, Geosci. Model Develop. Discuss., submitted, GMD-2010-23, 2010.

Nassar, R., Jones, D. B. A., Kulawik, S. S., et al.: Quantifying CO_2 sources and sinks with space-based CO_2 observations, in preparation, 2010.

Olsen, E.: Validation of Six Years of Mid-Tropospheric CO_2 Data from AIRS, NASA Sounder Science Team Meeting, Pasadena, CA, 4–7 May, 2009.

Osterman, G. B., Kulawik, S. S., Worden, H. M., Richards, N. A. D., Fisher, B. M., Eldering, A., Shephard, M. W., Froidevaux, L., Labow, G., Luo, M., Herman, R. L., Bowman, K. W., and Thompson, A. M.: Validation of Tropospheric Emission Spectrometer (TES) measurements of the total, stratospheric, and tropospheric column abundance of ozone, J. Geophys. Res.-Atmos., 113(D15), D15S16, doi:10.1029/2007JD008801, 2008.

Osterman, G. B., Bowman, K., Eldering, A., Fisher, B., Herman, R., Jacob, D., Jourdain, L., Kulawik, S., Luo, M., Monarrez, R., Osterman, G., Paradise, S., Payne, V., Poosti, S., Richards, N., Rider, D., Shepard, D., Shephard, M., Vilnrotter, F., Worden, H., Worden, J., Yun, H., and Zhang, L.: Tropospheric Emission Spectrometer TES L2 Data User's Guide, Version 4.0, Pasadena, Jet Propulsion Laboratory/California Institute of Technology, 2009.

Pak, B. C. and Prather, M. J.: CO_2 source inversions using satellite observations of the upper troposphere, Geophys. Res. Lett., 28(24), 4571–4574, 2001.

Palmer, P. I., Jacob, D. J., Jones, D. B. A., Heald, C. L., Yantosca, R. M., Logan, J. A., Sachse, G. W., and Streets, D. G.: Inverting for emissions of carbon monoxide from Asia using aircraft observations over the western Pacific, J. Geophys. Res.-Atmos., 108(D21), 8828, doi:10.1029/2003JD003397, 2003.

Payne, V. H., Clough, S. A., Shephard, M. W., Nassar, R., and Logan, J. A.: Information-centered representation of retrievals with limited degrees of freedom for signal: Application to methane from the Tropospheric Emission Spectrometer, J. Geophys. Res.-Atmos., 114, D10307, doi:10.1029/2008JD010155, 2009.

Raupach, M.R., Marland, G., Ciais, P., Le Quere, C., Canadell, J. G., Klepper, G., and Field, C. B.: Global and regional drivers of accelerating CO_2 emissions, P. Natl. Acad. Sci., 104(24), 10288–10293, doi:10.1073/pnas.0700609104, 2007.

Rayner, P. J., Enting, I. G., and Trudinger, C. M.: Optimizing the CO_2 observing network for constraining sources and sinks, Tellus B, 48(4), 433–444, 1996.

Rayner, P. J. and O'Brien, D. M.: The utility of remotely sensed CO_2 concentration data in surface source inversions, Geophys. Res. Lett., 28(1), 175–178, 2001.

Richards, N. A. D., Osterman, G. B., Browell, E. V., Hair, J. W., Avery, M., and Li, Q. B.: Validation of Tropospheric Emission Spectrometer ozone profiles with aircraft observations during the intercontinental chemical transport experiment-B, J. Geophys. Res.-Atmos., 113(D16), D16S29, doi:10.1029/2007JD008815, 2008.

Riley, W. J., Biraud, S. C., Torn, M. S., Fischer, M. L., Billesbach, D. P., and Berry, J. A.: Regional CO_2 and latent heat surface fluxes in the Southern Great Plains: Measurements, modeling, and scaling, J. Geophys. Res., in press, 2009.

Rinsland, C. P., Luo, M., Logan, J. A., Beer, R., Worden, H., Kulawik, S. S., Rider, D., Osterman, G., Gunson, M., Eldering, A., Goldman, A., Shephard, M., Clough, S. A., Rodgers, C., Lampel, M., and Chiou, L.: Nadir measurements of carbon monoxide distributions by the Tropospheric Emission Spectrometer instrument onboard the Aura Spacecraft: Overview of analysis approach and examples of initial results, Geophys. Res. Lett., 33(22), L22806, doi:10.1029/2006GL027000, 2006.

Shephard, M. W., Worden, H. M., Cady-Pereira, K. E., Lampel, M., Luo, M., Bowman, K. W., Sarkissian, E., Beer, R., Rider, D. M., Tobin, D. C., Revercomb, H. E., Fisher, B. M., Tremblay, D., Clough, S. A., Osterman, G. B., and Gunson, M.: Tropospheric Emission Spectrometer nadir spectral radiance comparisons, J. Geophys. Res., 113, D15S05, doi:10.1029/2007JD008856, 2008.

Stephens, B. B., Gurney, K. R., Tans, P. P., Sweeney, C., Peters, W., Bruhwiler, L., Ciais, P., Ramonet, M., Bousquet, P., Nakazawa, T., Aoki, S., Machida, T., Inoue, G., Vinnichenko, N., Lloyd, J., Jordan, A., Heimann, M., Shibistova, O., Langenfelds, R. L., Steele, L. P., Francey, R. J., and Denning, A. S.: Weak northern and strong tropical land carbon uptake from vertical profiles of atmospheric CO_2, Science, 316(5832), 1732–1735, 2007.

Strow, L. L. and Hannon, S. E.: A 4-year zonal climatology of lower tropospheric CO_2 derived from ocean-only Atmospheric Infrared Sounder observations, J. Geophys. Res.-Atmos., 113(D18), D18302, doi:10.1029/2007JD009713, 2008.

Suntharalingam, P., Spivakovsky, C. M., Logan, J. A., and McElroy, M. B.: Estimating the distribution of terrestrial CO_2 sources and sinks from atmospheric measurements: Sensitivity to configuration of the observation network, J. Geophys. Res.-Atmos., 108(D15), 4452, doi:10.1029/2002JD002207, 2003.

Suntharalingam, P., Jacob, D. J., Palmer, P. I., Logan, J. A., Yantosca, R. M., Xiao, Y. P., Evans, M. J., Streets, D. G., Vay, S. L., and Sachse, G. W.: Improved quantification of Chinese carbon fluxes using CO_2/CO correlations in Asian outflow, J. Geophys. Res.-Atmos., 109(D18), D18S18, doi:10.1029/2003JD004362, 2004.

Tans, P. P., Fung, I. Y., and Takahashi, T.: Observational Constraints on the Global Atmospheric CO_2 Budget, Science, 247(4949), 1431–1438, 1990.

Tans, P. P. and Conway, T. J.: Monthly atmospheric CO_2 mixing ratios from the NOAA CMDL carbon cycle cooperative global air sampling network, 1968–2002, a Compendium of Data on Global Change, Carbon Dioxide Inf. Anal. Center, Oak Ridge, Tenn., Oak Ridge Natl. Lab., US Dep. of Energy., 2005.

Wang, H., Jacob, D. J., Kopacz, M., Jones, D. B. A., Suntharalingam, P., Fisher, J. A., Nassar, R., Pawson, S., and Nielsen, J. E.: Error correlation between CO_2 and CO as constraint for CO_2 flux inversions using satellite data, Atmos. Chem. Phys., 9, 7313–7323, doi:10.5194/acp-9-7313-2009, 2009.

Worden, J., Kulawik, S. S., Shephard, M. W., Clough, S. A., Worden, H., Bowman, K., and Goldman, A.: Predicted errors of tropospheric emission spectrometer nadir retrievals from spectral window selection, J. Geophys. Res.-Atmos., 109(D9), D09308, doi:10.1029/2004JD004522, 2004.

Worden, H. M., Logan, J. A., Worden, J. R., Beer, R., Bowman, K., Clough, S. A., Eldering, A., Fisher, B. M., Gunson, M. R., Herman, R. L., Kulawik, S. S., Lampel, M. C., Luo, M., Megretskaia, I. A., Osterman, G. B., and Shephard, M. W.: Comparisons of Tropospheric Emission Spectrometer (TES) ozone profiles to ozonesondes: Methods and initial results, J. Geophys. Res.-Atmos., 112(D3), D03309, doi:10.1029/2006JD007258, 2007.

Yokota, T., Yoshida, Y., Eguchi, N., Ota, Y., Tanaka, T., Watanabe, H., and Maksyutov, S.: Global Concentrations of CO$_2$ and CH$_4$ Retreived from GOSAT: first Preliminary Results, Sci. Online Lett. Atmos., 5, 160–163, doi:10.2151/sola.2009-041, 2009.